Lithos 318–319 (2018) 448–463

Contents lists available at ScienceDirect

Lithos

journal homepage: www.elsevier.com/locate/lithos

Preservation of systematic Ni and Cr heterogeneity in otherwise homogeneous mantle olivine: Implications for timescales of post-metasomatism re-equilibration

Charlotte G. Jackson *, Sally A. Gibson

Department of Earth Sciences, University of Cambridge, Downing St, Cambridge CB2 3EQ, UK

ARTICLE INFO

Article history:
Received 11 May 2018
Accepted 21 August 2018
Available online 28 August 2018

Keywords:
Diffusion in olivine
Metasomatism
Crystallographic anisotropy
Kimberlite
Mantle xenolith

ABSTRACT

The flux of elements into Earth's sub-continental lithospheric mantle is facilitated by the passage of small-fraction melts that either crystallise new phases or react with pre-existing minerals.Metasomatised peridotite records the end product of this exchange but rarely captures the process in the act due to subsolidus re-equilibration. We present the results of a systematic investigation of a metasomatic melt channel preserved in a mantle peridotite from the Late Cretaceous Bultfontein kimberlite (Kaapvaal craton) that shows rare direct evidence of the melt-rock reaction processes. We show that the metasomatic proto-kimberlite melt underwent variable crystallisation of clinopyroxene, sulfides, phlogopite, spinel and zircon together with interaction and diffusive exchange with the surrounding olivine-rich mantle.

Element profiles across large olivine porphyroclasts (Fo_{88}) show significant core-to-rim variations in Ni (NiO = 0.18–0.32 wt%) and Cr (Cr = 35–60 ppm), while concentrations of all other elements (e.g. Mg, Fe, Mn, Co, V)are remarkably homogeneous. Electron backscatter diffraction analysis shows that the disequilibrium of Ni and Cr is greatest where the crystal contains large components of the [100] and [010] axes. The disequilibrium is preserved in certain orientations because diffusion of Ni and Cr in olivine is more anisotropic than Fe-Mg and Mn, and slower in the [100] and [010] directions. We present the first observations of Ni and Cr decoupling from other elements in mantle olivine and suggest that this is a consequence of: (i)changing mineral-melt concentration gradients associated with the reactive percolation of a precursory kimberlite melt; and (ii) late-stage sulfide and spinel precipitation.

We use the diffusion limited re-equilibration of Ni in olivine to quantify the timing of metasomatism prior to xenolith entrainment by the host kimberlite. Our modelling indicates that reactive percolation occurred on the order of 10^3–10^5 years prior to entrainment; this provides an additional line of support for the hypothesis that a period of metasomatism by proto-kimberlite melts precedes the final kimberlite ascent to the surface. The broader implication of our finding of variable rates of minor element diffusion in natural olivine is that it highlights the importance of anisotropy and the impact of changing local concentration gradients during subsolidus re-equilibration.

1. Introduction

The sub-continental lithospheric mantle represents one of Earth's largest and most long-lived chemical reservoirs. Direct evidence from mantle xenoliths shows that beneath the ancient cores of continents a once refractory melt residue has undergone billions of years of refertilization (Gibson et al., 2008; Menzies and Hawkesworth, 1986; Pearson, 1995; Shu and Brey, 2015; Simon et al., 2007; Woodhead et al., 2017). This long-term metasomatic enrichment results from reactive percolation of low-viscosity melts, such as kimberlites and carbonatites (e.g. van Achterbergh et al., 2001; Dawson, 1981; J.B. Dawson and Smith, 1977; Giuliani et al., 2014b; McKenzie, 1989; Rehfeldt et al., 2007). These small-fraction melts are highly charged with volatiles, including CO_2 and H_2O, and cause fracturing of the sub-cratonic mantle that may facilitate channelized flow of subsequent kimberlite melts (e.g. Aulbach et al., 2017; Giuliani et al., 2016, 2014).

Mantle metasomatism via reactive percolation of enriched melts may result in: (i) changes in modal mineralogy (modal/patent metasomatism; Harte, 1983); (ii) chemical changes with no accompanying mineralogical change (cryptic metasomatism; Dawson, 1984); or (iii) refertilisation of mantle peridotite (stealth metasomatism; O'Reilly and Griffin, 2013). Numerous studies have attempted to date metasomatic events using radiometric dating techniques on metasomatic

* Corresponding author.
E-mail address: cj340@cam.ac.uk (C.G. Jackson).

https://doi.org/10.1016/j.lithos.2018.08.026
0024-4937/

phases such as zircon and titanite. The highest precision are U-Pb dates on mantle zircons which indicate that they precipitate from metasomatic melts within several million years of kimberlite emplacement at the surface. Some of these U-Pb zircon ages are coeval with the host kimberlite (Kinny and Dawson, 1992; Konzett et al., 2013, 2000, 1998) while others are much older (Giuliani et al., 2015, 2014b; Liati et al., 2004; Woodhead et al., 2017). The episodic versus continuous nature, timescales and extent over which metasomatic interactions occur in the sub-continental mantle are, however, poorly constrained. The limitation of radiometric dating techniques is their resolution to an order of millions of years which cannot tell us whether a metasomatic event was related directly to the host kimberlite or not.

Higher resolution inferences about the timing of metasomatic events in the mantle are reliant on mineral disequilibrium and diffusion timescales. In the deep lithosphere the timescales of re-equilibration for minerals present in the refractory wall rocks of melt channels (e.g. garnet, olivine and orthopyroxene) are fast ($<10^5$ years, e.g. Griffin et al., 1996) so that each crystal only records the most recent chemical perturbation. At shallower levels, the re-equilibration timescales are longer, so the preservation of elemental zoning is more likely. Samples of mantle material entrained during the short re-equilibration time therefore potentially preserve diffusion profiles in minerals that can be used to estimate the timing of metasomatism prior to kimberlite emplacement.

Here we present high-resolution in-situ micro-analyses of major and trace elements in rare, un-equilibrated, olivines found in a metasomatised peridotite from Bultfontein Mine, South Africa. By combining olivine diffusion profiles for a range of major (Mg, Fe), minor and trace elements (Ni, Mn, Cr, Co, Cu, Ti, V and Zn) with crystallographic controls we show how Ni and Cr disequilibrium can be preserved in otherwise homogeneous mantle olivines. We use diffusion modelling of Ni in olivine to quantify the timescales of equilibration of refractory wall rock following reactive percolation of metasomatic melts through subcratonic lithospheric mantle.

2. Description of veined mantle peridotite BD3067, Bultfontein

Our study focusses on a large fragment of veined mantle peridotite (BD3067) entrained by the Bultfontein Group I kimberlite in Kimberley (S. Africa). The emplacement of this pipe at 84 (± 0.9) Ma (Kramers et al., 1983) was coeval with widespread Group I kimberlite activity across the southern Kaapvaal craton (Griffin et al., 2014). Numerous previous studies have shown that the Bultfontein kimberlite sampledhighly-heterogeneous and extensively-metasomatised mantle (e.g. Erlank, 1987; Giuliani et al., 2013a, 2013b; Jones et al., 1982; Kramers et al., 1983; Rehfeldt et al., 2007; Simon et al., 2007). Mineral separates from a suite of Bultfontein xenoliths (including BD3067) were initially analysed for REEs, together with Sr-Rb, Sm-Nd and Pb isotopes, by Kramers et al. (1983). They concluded that a kimberlite melt, which preceded emplacement of the Bultfontein kimberlite, was responsible for the metasomatism. Our study builds on this work by carrying out systematic in-situ analyses of major, trace and minor elements in minerals from one of these samples, BD3067. We combine these results with a petrographic and microstructural study in order to quantify the timescales of mineral equilibration and length scales of metasomatism.

Mantle xenolith BD3067 contains a spectacular, bright green, trichotomous branching, clinopyroxene-rich vein set in a matrix of olivine porphyroclasts and neoblasts (Fig. 1a and b). Orthopyroxene is absent, and the vein host rock is a dunite. At its widest point, the clinopyroxene-rich vein measures 45 mm. Branch terminations and regions of more isolated clinopyroxene crystallisation are associated with small amounts of phlogopite. The large olivine porphyroclasts and clinopyroxenes (both 2–6 mm diameter) show significant internal deformation, exhibited in olivine subgrains, recrystallisation and complex fine structures (Fig. 1c and d). Accessory phases include large anhedral zircons (up to 5 mm diameter; Fig. 1e) and very small amounts of Cr-spinel that have crystallised within the main vein. Away from this region we observe phlogopite, large (0.2–4 mm) Fe-Ni sulfides, interstitial amongst the small (<50 μm) olivine neoblasts, and ilmenite.

Multiple thin sections were made from xenolith BD3067, including across the main vein and regions further from it (Fig. 1a).

3. Mineral chemistry of veined mantle peridotite BD3067

Olivine, clinopyroxene, phlogopite and sulfides were analysed for major and minor elements using a Cameca SX100 electron probe microanalyser (EPMA). Minor and trace element concentrations were determined on the same grains with an ESI UP193UC laser inductively coupled to a Nexion 350D quadruple mass spectrometer (LA-ICP-MS). All of these analyses were undertaken in the Department of Earth Sciences at the University of Cambridge. Further details of these analytical setups are provided in Supplementary File A. Representative clinopyroxene and olivine compositions are provided in Tables 1 and 2, respectively, sulfide compositions are given in Table 3 and all analyses in Supplementary File B.

3.1. Clinopyroxene

The clinopyroxenes in BD3067 have a high Mg number (Mg# = 89–93, average Mg# 91.1 ± 1.8 (2σ), $n = 45$) and CaO content (22 ± 0.7 wt%, n = 45) and are diopsides (Table 1; Fig. 2). They have low TiO_2 (0.20 ± 0.03 wt%, n = 45) and Na_2O (1.23 ± 0.37 wt%, n = 45), and very low Al_2O_3 contents (0.63 ± 0.15 wt%, n = 45). Diopsides in the main vein have lower Cr_2O_3 (0.74 ± 0.14 wt%, $n = 15$) and higher FeO (3.08 ± 0.25 wt%, Mg# = 90.6 ± 0.75, n = 15) than those further away (Cr_2O_3 = 0.98 ± 0.86 wt%; FeO = 2.89 ± 0.58 wt%; Mg# = 91.1 ± 1.78, $n = 10$). This relationship is illustrated in Fig. 2. There is also a subtle difference in Ni content with the distal diopsides having a higher Ni content and greater variability (243 ± 110 ppm, n = 10) than those found in the vein (185 ± 23 ppm, n = 15).

The diopsides have remarkably high Zr (107 ± 38 ppm) and Hf (6.63 ± 2.85 ppm) concentrations so that primitive mantle normalised values are 10 and 24, respectively (Fig. 3). They are enriched in light rare earth elements (REE) with concentrations 3 to 8 times primitive mantle. The heavy REE contents of the diopsides are by comparison low and 4–5 times lower than primitive mantle. As a result, the diopsides have high La/Yb (12–17) and Zr/Hf (90–130), but very low Ti/Eu (1300–1600) compared to primitive mantle (McDonough and Sun, 1995). While the concentration of incompatible trace elements in diopsides in the main vein is more uniform, their composition lies within the wider range of pyroxenes away from the main vein.

3.2. Olivine

The olivine neoblasts (nb) and porphyroclasts (pc) in BD3067 are characterised by uniform but moderate forsterite contents (nbMg# = 88.0 ± 0.36, $n = 14$; pc Mg# = 88.0 ± 0.22, $n = 12$, Table 2; Fig. 4). Both generations also have moderate MnO (nb = 0.15 ± 0.04 wt%, n = 14; pc = 0.16 ± 0.03 wt%, n = 12) but low CaO (≪0.1 wt%) concentrations. Similar to the diopsides, all of the olivines have extremely low contents of Al (8 ± 5 ppm, n = 12), and the neoblasts have low NiO (0.21 ± 0.05 wt%, n = 14).

The olivines in BD3067 have higher P (99 ± 35 ppm, $n = 9$), Ti (150 ± 23 ppm, n = 9) and Zn contents (105 ± 19 ppm, $n = 18$) but similar concentrations of V (3.9 ± 0.7 ppm), Co (133 ± 11.4 ppm) and Cu (1.3 ± 0.6 ppm) to those found in previous studies of mantle olivines (e.g. Aulbach et al., 2017; De Hoog et al., 2010). All of the olivine neoblasts are uniform in composition but a number of the large porphyroclasts have Ni- and Cr-rich cores and Ni- and Cr-poor rims. These rims have the same composition as the neoblasts and the un-zoned porphyroclasts (NiO = 0.20 ± 0.02 wt%, $n = 13$; Cr = 37 ± 6 ppm,

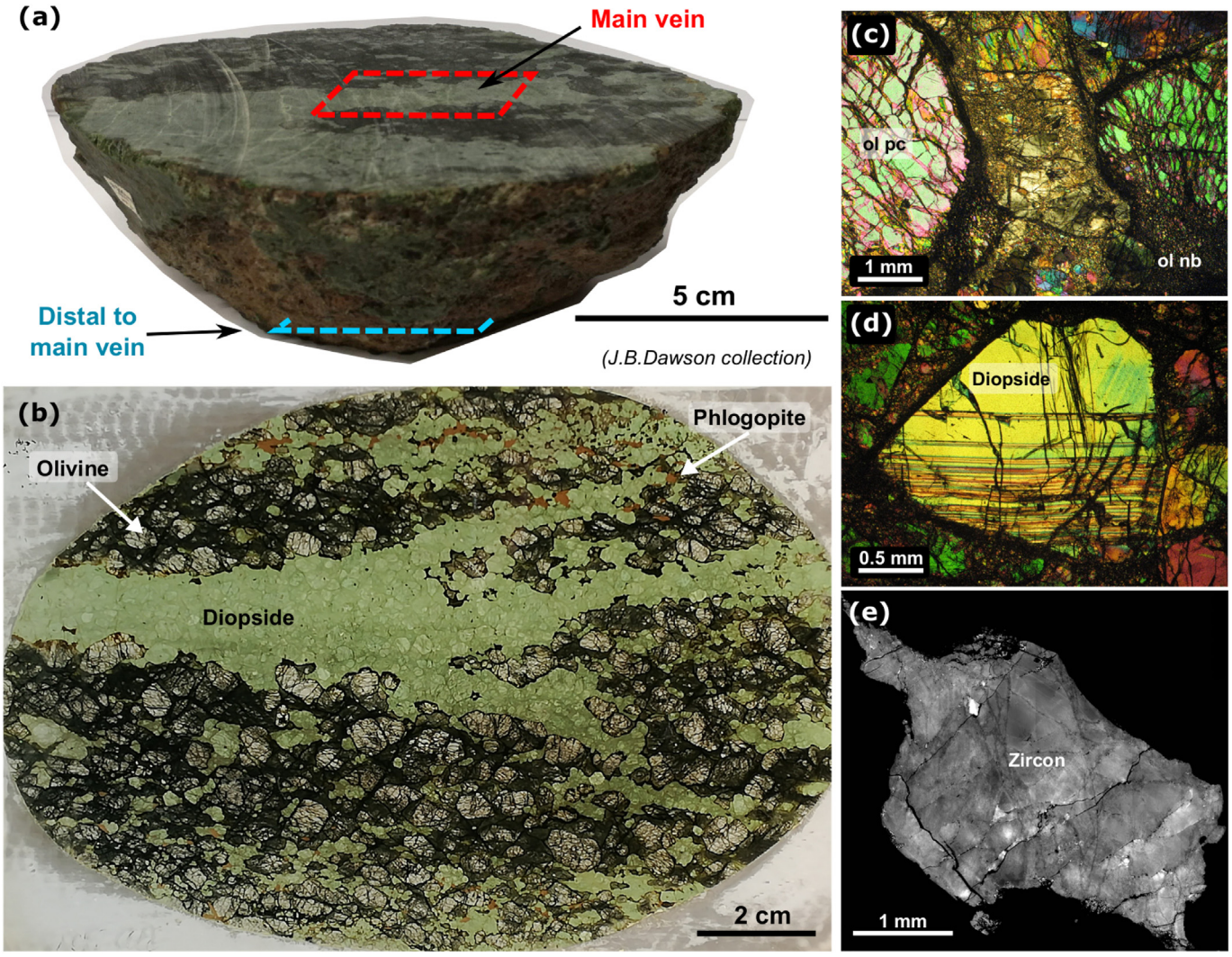

Fig. 1. Images of the veined xenolith BD3067. (a)Image of the hand specimen of mantle xenolith BD3067 together with locations of (b)the proximal and (c)distal sections as described in the main text.(b)Photograph of a large, 13 by 9 cm, thin section containing a trichotomously branching vein; (c)Photomicrographs of olivine porphyroclasts (ol pc) and neoblasts (ol nb) (cross polarised light); (d)Complex deformation in clinopyroxene (cross polarised light); (e)Cathodoluminescence image of large zircon crystal within the main vein.

n= 9). The cores of the zoned olivines show a range in Ni (0.20–0.33 wt% NiO), Cr(32–63 ppm) and Ti (117–204 ppm) contents but are uniform for every other element and the same composition as the neoblasts and un-zoned olivine. This is demonstrated by comparing the NiO and MnO contents in Fig. 4a and b.

We measured profiles of major and minor element concentrations across sixteen, large (2 to 6.3 mm), olivine porphyroclasts in BD3067. Six of these profiles are across olivines that border the main clinopyroxene vein (hereby referred to as proximal olivine). The remaining ten profiles are across porphyroclasts distal to the main vein (hereby referred to as distal olivine), where the proportion of clinopyroxene is lower and phlogopite and sulfides higher. Examples of representative profiles of elements across olivine porphyroclasts, determined by EPMA and LA-ICP-MS, in both the proximal and distal sections are shown in Fig. 5, and all profiles and analyses are presented in Supplementary File B.

An important finding arising from our study is that olivine porphyroclasts which border the main vein in BD3067 have homogeneous major and trace element compositions (e.g. Fig. 5d, OlivineM)whereas those away from this region (e.g. Olivine A, D)exhibit a range in Ni, Cr and Ti but have constant Si, Mg, Fe and Mn, Co, V and Zn contents. Fig. 4d and f show a positive correlation between Ni and Cr, and Ni and Ti, respectively. This reflects the zonation in these elements, however, the variation is not uniform across the olivine porphyroclasts: some show much stronger core-to-rim variation than others; some have parabolic zonation (e.g. Olivine A)and others more complex patterns. While the olivine crystals that exhibit zonation in Ni and Cr tend to be the largest, there are others of the same size that have homogeneous compositions. The gradient of the Ni and Cr profiles varies within and between crystals. Fig. 5 shows profiles for two endmembers: Olivine A has the most strongly zoned core-to-rim profile and Olivine B has uniform concentrations of NiO (0.2 wt%) and Cr(34ppm) that are the same as those in the neoblasts. The core composition in the unequilibrated profiles range from 0.28–0.34 wt% NiO, and 50–63 ppm Cr. By contrast the rim composition of the zoned olivines are strikingly uniform with 0.18–0.2 wt% NiO and 35–40 ppm Cr.The rims have the same chemical composition for all elements as the olivine neoblasts.

3.3. Sulfides

We observed several large, irregular, metasomatic Fe-Ni sulfides in the thin sections of BD3067 (Fig. 6). The shape, size and composition of these grains are extremely heterogeneous. Most of the sulfides have been heavily serpentinised to the low temperature assemblage of magnetite, heazlewoodite and serpentine (Lorand and Grégoire, 2006), but some unaltered areas remain. The composition of the unaltered regions

Table 1
Representative major, minor and trace element composition of clinopyroxene in BD3067.

Crystal	cpx_10/1	cpx_18/1	cpx_19/1	cpx_31/1	BD3067CPX1	BD3067CPX2	BD3067CPX4a	BD3067CPX5
Location[a]	NV	NV	NV	NV	V	V	V	V
EPMA (wt%)								
SiO_2	54.67	55.52	55.01	55.39	54.46	54.57	54.13	54.37
TiO_2	0.22	0.20	0.19	0.20	0.20	0.20	0.20	0.19
Al_2O_3	0.62	0.66	0.67	0.60	0.62	0.66	0.60	0.63
Cr_2O_3	1.85	1.13	0.80	0.83	0.74	0.73	0.85	0.59
FeO	2.85	3.02	3.01	2.62	3.04	3.00	3.11	2.98
MnO	0.06	0.09	0.09	0.10	–	–	–	–
MgO	15.90	16.23	16.68	16.69	16.55	16.65	16.61	16.71
NiO	b.d.l	b.d.l	b.d.l	b.d.l	0.02	0.02	0.02	0.02
CaO	21.60	22.17	21.97	22.52	22.19	22.21	22.00	22.17
Na_2O	1.49	1.25	1.10	1.11	1.22	1.09	1.22	1.15
Mg#	90.9	90.5	90.8	91.9	90.6	90.8	90.5	90.9
LA-ICP-MS (ppm)								
Al	3264	3179	3571	3448	3478	3438	3470	3516
Sc	38.8	43.4	54.5	53.9	57.0	54.3	52.0	54.4
Ti	1046	1023	1061	1144	1239	1256	1398	1356
V	261.3	328.3	432.7	418.8	373.3	359.2	353.0	391.5
Co	18.70	21.50	19.83	22.06	18.65	17.96	18.38	19.55
Ni	350.8	231.8	248.9	250.6	177.5	176.3	197.8	163.8
Sr	171.2	219.6	154.9	203.6	153.3	161.2	158.6	146.2
Y	4.96	4.70	3.93	5.30	3.97	3.89	4.37	4.25
Zr	139.6	110.4	109.8	121.9	99.7	85.8	109.6	92.9
Nb	0.38	0.91	0.88	1.62	0.209	0.187	0.374	0.209
La	2.44	3.84	3.24	4.89	2.21	2.45	2.65	2.16
Ce	12.23	17.15	13.67	19.88	10.22	11.46	11.76	10.20
Pr	2.12	2.89	2.34	3.18	2.002	2.233	2.233	1.947
Nd	11.24	14.61	11.61	15.57	10.98	11.97	12.34	10.81
Sm	2.93	3.67	2.91	3.66	2.816	3.036	3.256	2.926
Eu	0.98	1.13	0.87	1.20	0.891	0.902	0.924	0.913
Gd	2.46	2.89	1.97	2.83	2.398	2.42	2.563	2.486
Tb	0.327	0.340	0.263	0.367	0.264	0.297	0.308	0.297
Dy	1.59	1.59	1.35	1.61	1.34	1.34	1.46	1.40
Ho	0.225	0.202	0.176	0.238	0.176	0.187	0.198	0.22
Er	0.486	0.435	0.335	0.387	0.341	0.33	0.363	0.396
Tm	0.046	0.036	0.038	0.040	0.033	0.033	0.033	0.033
Yb	0.204	0.160	0.207	0.196	0.143	0.143	0.187	0.165
Lu	0.019	0.016	0.014	0.018	0.011	0.011	0.022	0.022
Hf	7.56	6.16	6.85	6.86	6.28	5.25	6.70	5.83
Ta	0.017	0.045	0.052	0.083	0.011	0.011	0.022	0.022
Pb	0.272	0.416	0.403	0.507	0.308	0.264	0.308	0.264

[a] NV = not in main vein; V = in main vein; b.d.l = below detection limit; — not measured.

of the sulfides are shown in Table 3. The heterogeneity in composition is especially prevalent in Cu and Ni. Some regions have higher Cu content; however a low Cu concentration is common in Kaapvaal peridotite mono-sulfide-solution and demonstrates that they have re-equilibrated at a low temperature (Lorand and Grégoire, 2006). There also appear to beexsolution lamellae in the sulfides that are often Ni-rich (up to 44 wt% NiS).

3.4. Zircon

Energy Dispersive X-ray Spectroscopy (EDS) major element mapping of the largest zircon, which is present in a bottlenecked region of the main vein and adjacent to olivine porphyroclasts, shows that it is unzoned but regions of baddeleyite (ZrO_2) are present adjacent to cracks in the crystal.

4. Crystal orientation of olivine

Previous studies of element diffusivity in olivine have highlighted the importance of crystal orientation (e.g. Costa and Morgan, 2010; Dohmen and Chakraborty, 2007; Spandler and O'Neill, 2010). We used a FEI Quanta 650FEG SEM equipped with a Bruker e- Flash HR Electron Back-Scatter Diffraction (EBSD) detector in the Department of Earth Sciences at the University of Cambridge to make EBSD maps of variably equilibrated olivine porphyroclasts in veined xenolith BD3067, in regions parallel to the electron microprobe and LA-ICP-MS profiles. We used the EBSD data to calculate the orientation of crystals in the thin sections, i.e. angles of the plane to the ⟨100⟩ axes. These reveal that the angle between the crystal face and the position of the [001] axis correlates with the level of heterogeneity in Ni and Cr in olivines distal to the vein (Fig. 7). This is significant because diffusion of major and minor elements in olivine is anisotropic and faster along the [001] axis than the [100] and [010] axes (Dohmen and Chakraborty, 2007). The proximal olivines are all homogeneous, regardless of the crystallographic orientation.

Fig. 7 shows the correlation between the range in NiO across the crystal and the angle between the profile and the [001] fast diffusion axis. The profiles taken in crystals normal to the [001] axis show the greatest degree of heterogeneity, for example Olivines A and D(Fig. 5a and c), whereas the most equilibrated profile in the distal sections (across Olivine B)is parallel to the [001] axis. There are a number of intermediate levels of equilibration that also reflect the angle of the cut plane.

5. Calculated and inferred melt chemistry

Olivines found in lithospheric mantle peridotites typically have NiO concentrations of 0.34–0.43 wt% that remain roughly constant over a range of Fo contents (Foley et al., 2013 and references therein; Bussweiler et al., 2015). The peak NiO concentration in the parabolic

Table 2
Representative major, minor and trace elements of olivine porphyroclasts and neoblasts in BD3067.

Crystal	olivine_a	olivine_a	olivine_b	olivine_b	olivine_d	olivine_d	olivine_g	olivine_g
Location	distal	distal	distal	distal	distal	distal	distal	distal
pc/nb[a]	pc	pc	pc	pc	pc	pc	pc	pc
position	core	rim	core	rim	core	rim	core	rim
EPMA (wt%)								
MgO	47.16	50.00	47.12	47.26	48.11	47.82	47.45	47.46
SiO_2	40.62	43.25	40.64	40.73	40.66	40.22	39.92	39.78
CaO	b.d.l	0.09	b.d.l	b.d.l	b.d.l	b.d.l	b.d.l	b.d.l
NiO	0.32	0.21	0.21	0.18	0.30	0.20	0.28	0.21
MnO	0.14	0.15	0.18	0.16	0.19	0.16	0.17	0.15
FeO	11.36	11.31	11.57	11.61	11.65	11.62	11.60	11.47
Fo	88.1	88.7	87.9	87.9	88.0	88.0	87.9	88.1
LA-ICP-MS (ppm)								
Na	88.6	56.3	58.5	89.3	85.2	65.1	67.4	47.5
Al	7.99	7.87	3.70	7.00	10.54	6.35	9.07	7.71
P	87.6	77.6	100.4	116.8	104.7	85.7	116.1	56.5
Sc	1.55	1.68	1.40	1.54	1.31	1.28	1.80	1.83
Ti	168.9	145.6	135.3	148.0	143.9	125.0	154.0	141.3
V	3.72	3.81	3.47	3.67	3.44	3.51	3.71	4.09
Cr	52.7	37.8	34.1	35.4	49.0	32.6	42.4	37.9
Mn	1038	1038	1042	1117	1053	966	1059	1060
Co	129.6	136.3	128.6	140.0	133.7	120.0	136.9	134.6
Ni	2157	1526	1438	1538	2089	1381	1905	1523
Cu	1.07	1.14	1.12	1.07	1.12	1.14	0.93	1.19
Zn	104.1	105.3	96.8	109.2	102.5	91.1	122.2	112.5
Y	0.0331	0.0196	b.d.l	0.0291	0.046	b.d.l	b.d.l	b.d.l
Zr	0.592	0.288	0.412	0.629	0.549	0.345	0.398	0.466
Nb	0.521	0.289	0.267	0.442	0.584	0.298	0.33	0.257
Sn	0.74	0.737	0.642	0.834	0.577	0.627	0.979	0.766
Pb	0.013	b.d.l	b.d.l	0.012	b.d.l	0.008	b.d.l	0.021

Crystal	tk5_1	tk4_1	tk4_4	tk4_12	olivine_m	olivine_m	olivine_n	olivine_n
Location	distal	distal	distal	distal	proximal	proximal	proximal	proximal
pc/nb	nb	nb	nb	nb	pc	pc	pc	pc
position					core	rim	core	rim
EPMA (wt%)								
MgO	47.69	47.41	47.50	47.52	48.08	47.49	47.69	47.83
SiO_2	41.10	40.32	40.44	40.63	40.24	40.86	40.45	40.53
CaO	b.d.l	b.d.l	b.d.l	b.d.l	0.03	b.d.l	b.d.l	0.04
NiO	0.22	0.20	0.19	0.23	0.20	0.20	0.20	0.20
MnO	0.14	0.17	0.11	0.16	0.15	0.14	0.16	0.15
FeO	11.59	11.33	11.43	11.55	11.62	11.49	11.39	11.89
Fo	88.0	88.2	88.1	88.0	88.1	88.0	88.2	87.8

[a] pc = porphyroclast; nb = neoblast; b.d.l = below detection limit.

profiles (0.34 wt%) across olivine porphyroclasts in the veined Bultfontein xenolith BD3067 are similar to non-metasomatised mantle olivines (De Hoog et al., 2010; Foley et al., 2013). Fig. 8 compares the composition of the olivine neoblasts and porphyroclasts proximal and distal to the clinopyroxene vein with the composition of olivine cores and rims in kimberlitic olivine from the Kimberley region, as compiled by (Giuliani, 2018). The rims of the kimberlitic olivines represent magmatic olivine that has crystallised from the magma, and the cores represent xenocrystic mantle olivine (Giuliani, 2018). The BD3067 proximal olivine and the distal olivine neoblasts and porphyroclast rims have a NiO and Fo content that resembles the magmatic kimberlite rather than un-metasomatised mantle olivine. The olivine porphyroclast cores have higher NiO, similar to mantle olivine. The MnO content of all of the olivine crystals is very similar to the kimberlite magmatic olivine.

Table 3
Major element compositions of Ni-rich regions and exsolution lamellae in sulfides.

Section	Tk5	Tk4	Tk4	Tk4	Tk4	Tk4
Sulfide/Point	45/1	28/1	32/1	27/21	27/25	27/27
S (wt%)	18.93	12.45	15.75	16.65	20.20	27.13
Ni	24.60	11.63	15.53	21.26	28.19	34.33
Fe	53.19	74.36	60.71	55.69	50.51	32.69
Si	2.46	0.94	4.07	5.95	0.43	5.15
Cu	0.12	0.38	3.67	0.09	0.22	0.10
Cr	0.71	0.23	0.28	0.36	0.45	0.60
NiS (mol. %)	30.38	13.24	18.61	25.70	35.20	43.71
FeS	66.34	85.20	73.37	67.90	63.70	42.08

We have used experimentally-determined partition coefficients to calculate the incompatible trace element concentrations of melts in equilibrium with the diopsides in BD3067. Fig. 9 compares these to the composition of the Bultfontein kimberlite (Roex et al., 2003) and a global carbonatite average (Bizimis et al., 2003). The four different sets of partition coefficients used reflect four different melt compositions at mantle pressure and temperature: (i)a silicate melt (Suzuki et al., 2012); (ii) carbonatite melt (Dasgupta et al., 2009); (iii) kimberlite melt (Keshav et al., 2005); and (iv) a silico-carbonate melt (Girnis et al., 2013). The main differences between the sets of partition coefficients are revealed in the behaviour of the HFSE, especially Nb, Ta, Zr and Hf. The partition coefficients using kimberlite and silico-carbonate melts calculate the melt to be much more enriched in Zr and Hf than the silicate and carbonatite melts. The implication that the melt was enriched in Zr is supported by the abundance of large metasomatic

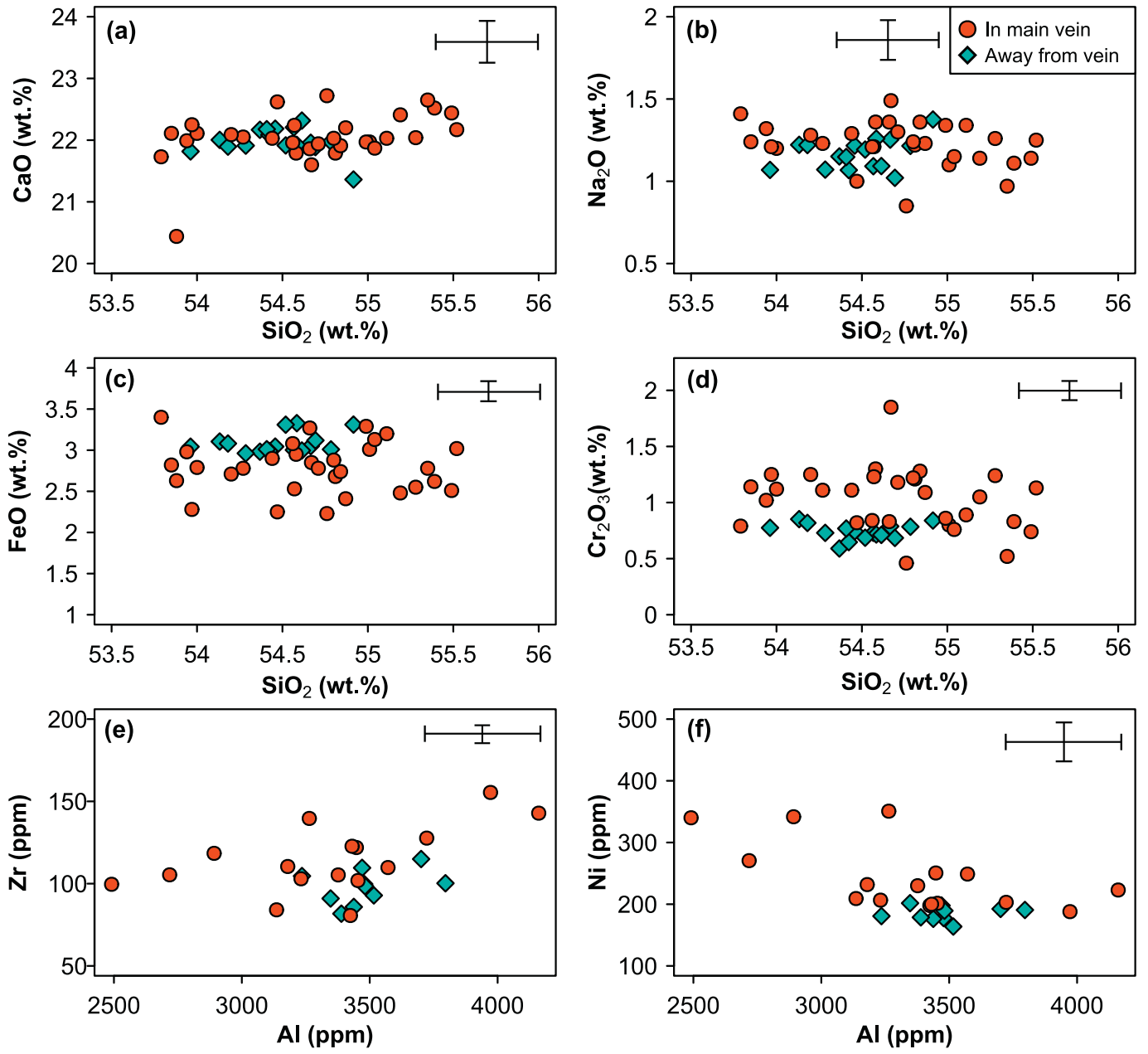

Fig. 2. Clinopyroxene variation diagrams (a)CaO vs. SiO_2; (b)Na_2O vs. SiO_2; (c)FeO vs. SiO_2; (d)Cr_2O_3 vs. SiO_2; (e)Ti vs. Al; (f)Ni vs. Al. Clinopyroxene from the main vein are plottedasred circles, and those away from the main vein in blue diamonds.

zircons in the vein (e.g. Fig. 1e). Of the cpx equilibrium melts calculated there is a good fit between the carbonatite cpx-melt and the Bultfontein kimberlite which matches the Zr/Hf ratio but differs in the Nb/Ta ratio. The silico-carbonatecpx-melt predicts the same Nb/Ta fractionation but no fractionation in Zr/Hf. Apart from the enrichment in Zr and Hf the silico-carbonate melt coefficients produce a good fit with the Bultfontein kimberlite. It is possible the composition of the Bultfontein kimberlite shown is depleted in Zr and Hf due to zircon fractionation.

The diopsides have very high Ca/Al, low Ti/Eu and high Zr/Hf ratios.These are often identified as features of carbonatite metasomatism (Rudnick et al., 1993), however the lack of magmatic carbonate and the abundance of a metasomatic silicate phase (diopside) implies that the metasomatic agent was not carbonatitic in nature. Instead we suggest that the melt was a silico-carbonate melt, consistent with the results of the recent study by Soltys et al. (2018) who reconstructed the parental composition of the Bultfontein kimberlite to be a transitional silicate-carbonate melt, and those of Simon et al., (2003) whose suggest clinopyroxene in mantle peridotite from the Kaapvaal is the product of metasomatism by kimberlite-like magmatism.

6. Mineral disequilibrium

Chemical disequilibrium is a common observation in mantle peridotites that have experienced metasomatism, but the decoupling of Ni and Cr disequilibrium from any other element in mantle olivine that we have observed is a unique and puzzling finding. The olivine profiles reported here do, however, show a broad similarity to profiles observed in olivines from the Springwater pallasite (Leitch et al., 1979; Zhou and Steele, 1993). In these meteoritic olivines, long wavelength diffusion profiles (mm scale) are observed in several elements, including Ni, Cr,

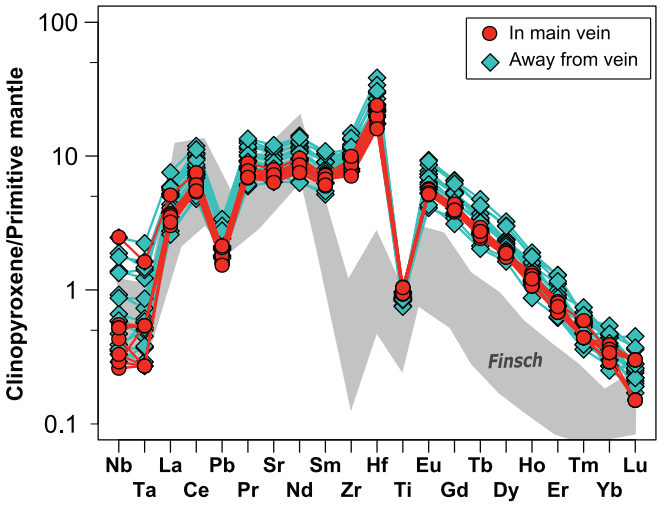

Fig. 3. Primitive mantle normalised trace-element plot of clinopyroxenes in BD3067. The composition of clinopyroxenes found in xenoliths from Finsch Mine are shown for comparison (Gibson et al., 2008).

Ca and Al, but flat profiles are observed in Fo content, Mn and V. In this case the outward diffusion of Ni and Cr is attributed to the decrease in the equilibrium concentration of the olivine with the adjacent metal phase, during cooling. The flat profiles are recognised as resulting from the lack of any other sink for these elements (e.g. V and Mn) outside of the olivine.

To our knowledge there has been no other study presenting decoupling of Ni and Cr from other elements in olivine. In BD3067 Ni and Cr are the only elements to show systematic core-to-rim variation although a few of the other minor elements show a degree of scatter. In some cases, for example Ti, this scatter weakly correlates with the Ni and Cr zoning (Fig. 4f). The core to rim multi-element decoupling, on millimetre length scales, indicates that these variations are not caused by overgrowth of olivine formed by fractionation of a crystallising melt, as is observed in olivine xenocrysts in kimberlite magmas (e.g. Arndt et al., 2010; Bussweiler et al., 2015; Giuliani et al., 2017; Pilbeam et al., 2013). It is unlikely that this is a growth effect due to the shape of the profile and the distance of the zoned olivines from the main vein, where the infiltrating melt would have facilitated growth. Instead, this is an effect of subsolidus re-equilibration.

No single factor can satisfactorily account for the observed decoupling, rather several aspects have produced, and influenced the preservation of the elemental patterns we see. These include: (i)mineral-melt and mineral-mineral concentration gradients during subsolidus re-equilibration; (ii) the presence of Ni/Cr stoichiometric phases; and (iii) anisotropy of diffusion in olivine. We suggest that the observed profiles are caused by an evolving melt composition and locally changing concentration gradients as new phases crystallise and change the local equilibrium conditions. The profiles represent the re-distribution of elements during subsolidus re-equiliibration(Cherniak and Liang, 2014, 2012), but the fact that we only see the profiles in Ni and Cr, and to a lesser extent Ti, is influenced by the local mineral assemblage and the diffusion of these elements in olivine; Ni and Cr because they exhibit strong anisotropic diffusion in olivine, and Ti because it's high charge makes diffusion very slow in olivine.

6.1. Concentration gradients: subsolidus re-equilibration

Re-equilibration during and after metasomatism is influenced by compositional differences and concentration gradients between: (i)the infiltrating melt; (ii) the pre-existing mantle phases; and (iii) the new metasomatic phases. We have established that the infiltrating melt was a silico-carbonate melt and suggest that this resorbed orthopyroxene and crystallised clinopyroxene (Lim et al., 2018; Simon et al., 2003). This early pulse of volatile-rich proto-kimberlite melt introduced a suite of elements into the system, altering the equilibrium conditions of the local mantle peridotite. Following the melt infiltration event, the new mineral assemblage required elemental re-distribution to re-equilibrate.

In the main vein of BD3067 the olivine and clinopyroxene are homogeneous. Equilibrated coexisting mantle olivine and clinopyroxene have the same Mg# ($K_D = 1$) (Pearson et al., 2003; Seckendorff and O'Neill, 1993). None of the olivine and clinopyroxene pairs in BD3067 are in equilibrium. In the main vein of BD3067, the homogeneous clinopyroxene and bordering olivine have Mg# of 90.6 ± 0.75 ($n = 15$) and 88.0 ± 0.21 ($n = 12$), respectively. The distal olivine porphyroclasts and the clinopyroxene away from the main vein are not equilibrated (cpx Mg# $= 91.1 \pm 1.78$, $n = 30$; olivine Mg# $= 88.0 \pm 0.36$, $n = 14$), and the clinopyroxenes show an even greater range in Mg#. As for Ni, based on a comparison with D_{Ni}^{ol-cpx} of close to 0.13 for equilibrated mantle xenoliths (Gibson et al., 2013; Stosch, 1981), we observe that the lower Ni, proximal clinopyroxenes (Ni $= 185 \pm 23$ ppm) are close to equilibrium with: (i)unzoned olivines; (ii) neoblasts; and (iii) porphyroclast rims (Ni $= 1548 \pm$ _271 ppm).

The clear differences between the levels of heterogeneity, and hence equilibration, in mineral grains in the main vein and the regions distal to it in BD3067 highlight controls of: (i)local temperature; (ii) concentration gradients; and (iii) mineral assemblage. The olivine porphyroclasts bordering the main vein all have homogeneous compositions (e.g. Olivine M in Fig. 4e). It is likely that the diffusivity of Ni in olivine and subsequent re-equilibration was increased near the vein due to the higher concentration gradients and temperatures associated with the larger volume of melt undergoing channelized flow (Griffin et al., 1996).

6.2. Late-stage crystallisation of accessory phases

Our data suggest that the olivine content became buffered at Fo_{88}, perhaps due to the resorption of orthopyroxene (Bussweiler et al., 2015; Giuliani et al., 2017; Pilbeam et al., 2013), but the Ni and Cr contents were still changing in response to the precipitation of late stage minerals such as sulfides and chrome-spinel and a lag in diffusion. We suggest that the infiltrating silico-carbonate melt was depleted in Ni (Roex et al., 2003; Soltys et al., 2018) and the Cr concentration will depend on the abundance of garnet in the melt source. The clinopyroxenes are not particularly enriched in Cr and Cr-spinel is only a minor phase in the vein assemblage, which implies that the melt was not significantly enriched in Cr.

A number of authors have suggested that an immiscible sulfide melt is produced at a late stage of kimberlite melt evolution (Giuliani et al., 2013a; Lorand and Grégoire, 2006) and Aulbach et al. (2017) attribute low Ni in mantle clinopyroxene from SW Greenland to concomitant sulfide saturation during metasomatism. For olivine to exchange Ni with sulfides, the latter must have initially been low in Ni. If the metasomatic agent was Ni-poor then it is possible that a Fe-Cu immiscible liquid separated from the melt and precipitated Fe-Cu base metal sulfides, as suggested by Lorand and Grégoire, (2006) for the origin of Fe-Cu-Base Metal Sulfides in phlogopite (±ilmenite ± rutile) peridotites. In the case of BD3067, the introduction of sulfides, a phase for which Ni is a stoichiometric component, shifted the distribution coefficients for the evolving mineral assemblage. As a result local chemical gradients changed depending on the resorbing or crystallising phases (e.g. Giuliani et al., 2014a); the late-stage crystallisation of Ni-poor sulfides catalysed Ni re-distribution and drove the Ni concentration down in olivine (e.g. Barnes et al., 2013). The sulfides are associated with olivine porphyroclasts, but there is no systematic spatial relationship between the position of the sulfides and the specific zoned olivine porphyroclasts. The lack of a close spatial relationship between the olivine and the sulfides suggests that there has been migration of Ni to

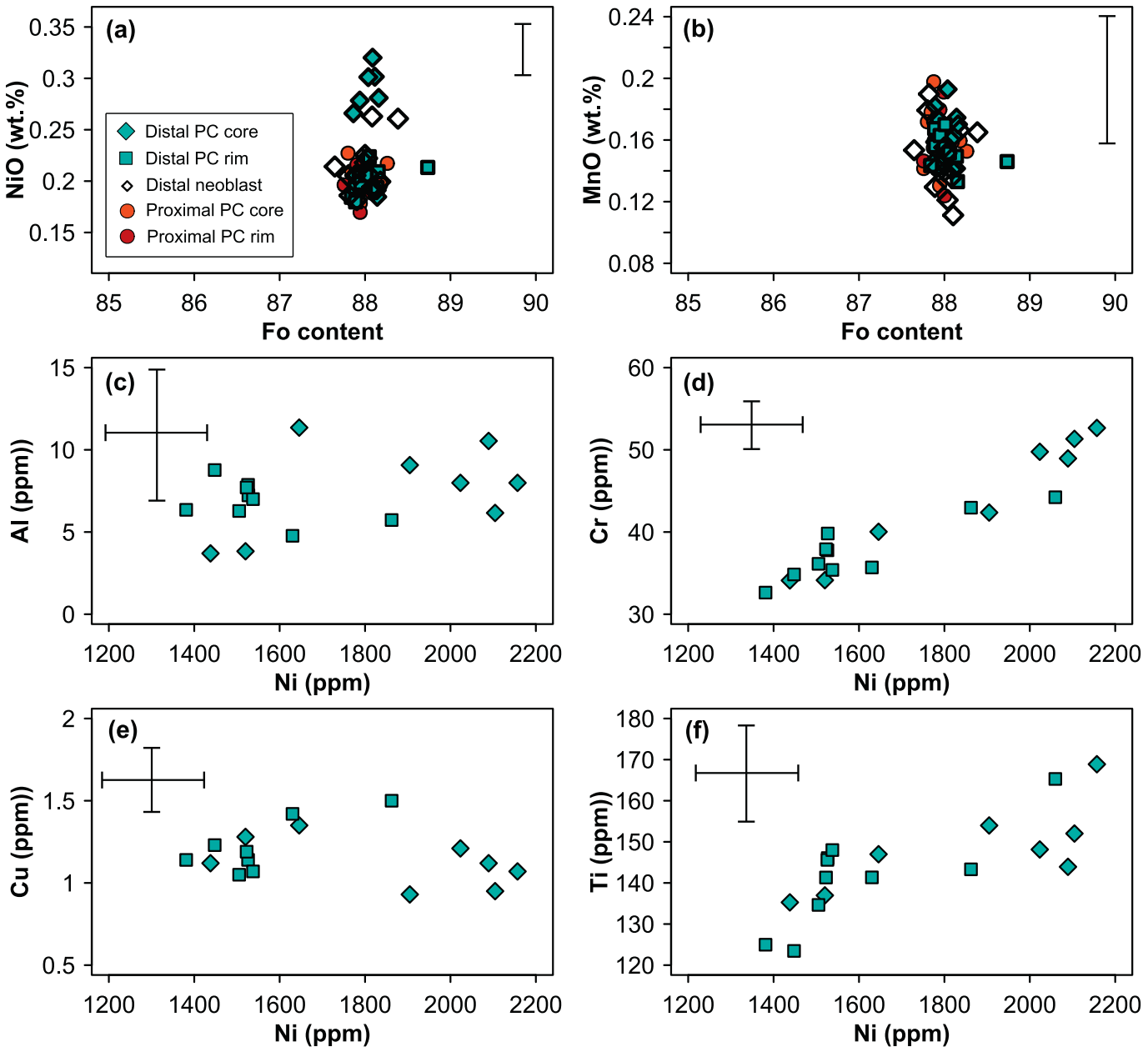

Fig. 4. Olivine variation diagrams (a)NiO vs. Fo content; (b)MnO vs. Fo content; (c)Al vs. Ni; (d)Cr vs. Ni; (e)Cu vs. Ni; (f)Ti vs. Ni. The legend in (a)reflects the textural and location (proximal or distal) of each measurement; pc stands for porphyroclast. NiO, MnO and Fo content have been measured using EPMA; Ni, Al, Cr, Cu, Ti have been measured using LA-ICP-MS. These are representative measurements that can be found in Supplementary File B.

distant sulfides facilitated by open grain boundaries and cracks in the old crystals; this sluggish solid-state diffusion is able to produce long wavelength, near-symmetrical profiles like those observed in this study (e.g. Leitch et al., 1979).The same systematic variation in Fe and Cu is not observed (other stoichiometric components of sulfides) and we suggest this is because the melt was enriched in Fe and Cu relative to the olivine. It is also possible that we do not see the same effect on Fe in olivine because Fe is a stoichiometric component of olivine and the effect would be negligible relative to that on Ni. If the sulfide melt was enriched in Cu (Lorand and Grégoire, 2006) there would be no concentration gradient to cause any Cu loss from olivine.

It is plausible that a similar mechanism has affected the redistribution of Cr and Ti. As aforementioned, we expect that the melt was not particularly enriched in Cr, and that most of the Cr was partitioned into diopside and Cr-spinel during crystallisation. The later stage melt, interacting with the distal olivine porphyroclasts, was therefore likely to be relatively Cr-poor. This reduced concentration gradient meant that re-equilibration was slower. Ti has also been affected by the crystallisation of diopside and ilmenite. With decreasing temperature (cooling post-metasomatism) Ti is preferentially partitioned from olivine to clinopyroxene (Witt-Eickschen and O'Neill, 2005) and during subsolidus re-equilibration Ti will diffuse out of olivine and into adjacent clinopyroxene (Cherniak and Liang, 2014). Ti diffuses very slowly in olivine due to its high charge, therefore explaining the sluggish re-equilibration.

6.3. Olivine diffusion anisotropy

The subsolidus re-equilibration of the metasomatic mineral assemblage in BD3067 has been achieved for many elements but the most systematic variation is observed in Ni and Cr. These elements have been slower to equilibrate than others, but only in some crystals. Part of

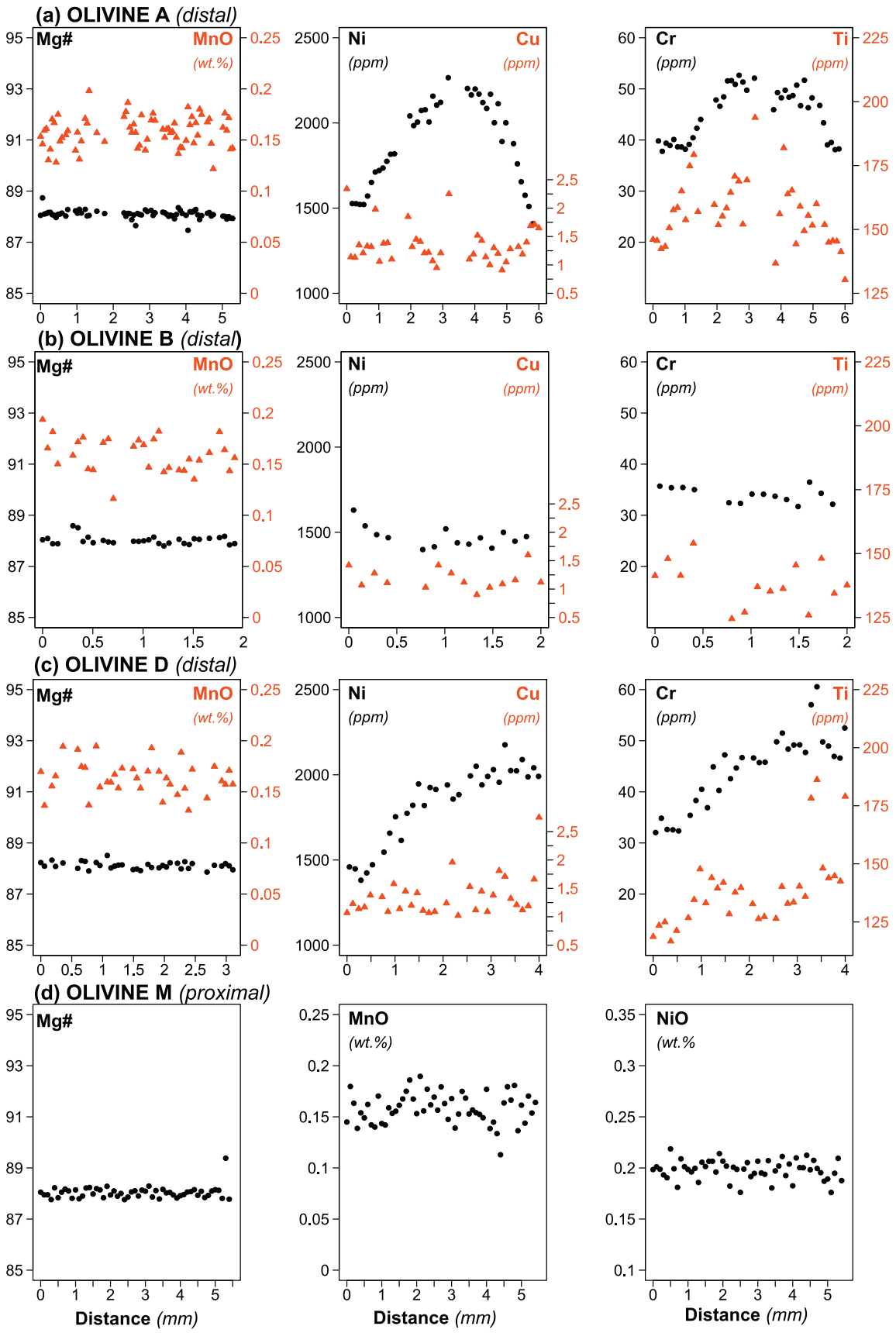

Fig. 5. Olivine profiles taken of rim to rim transects in four olivine crystals. Three distal olivines are shown (a)Olivine A; (b)Olivine B; (c)Olivine D, and one proximal olivine (d)Olivine M. The black circles represent the measurements for the y axis on the left-hand side (e.g. Mg# in column 1), and the red triangles are associated with the y axis on the right-hand side (e.g. MnO in column 1). Mg# (MgO/(MgO + FeO) mol) and MnO are measured using EPMA and Ni, Cu, Cr and Ti are LA-ICP-MS measurements. Olivines A and D show strong variation in Ni, Cr and Ti across the crystal whereas Olivines B and M are homogeneous.

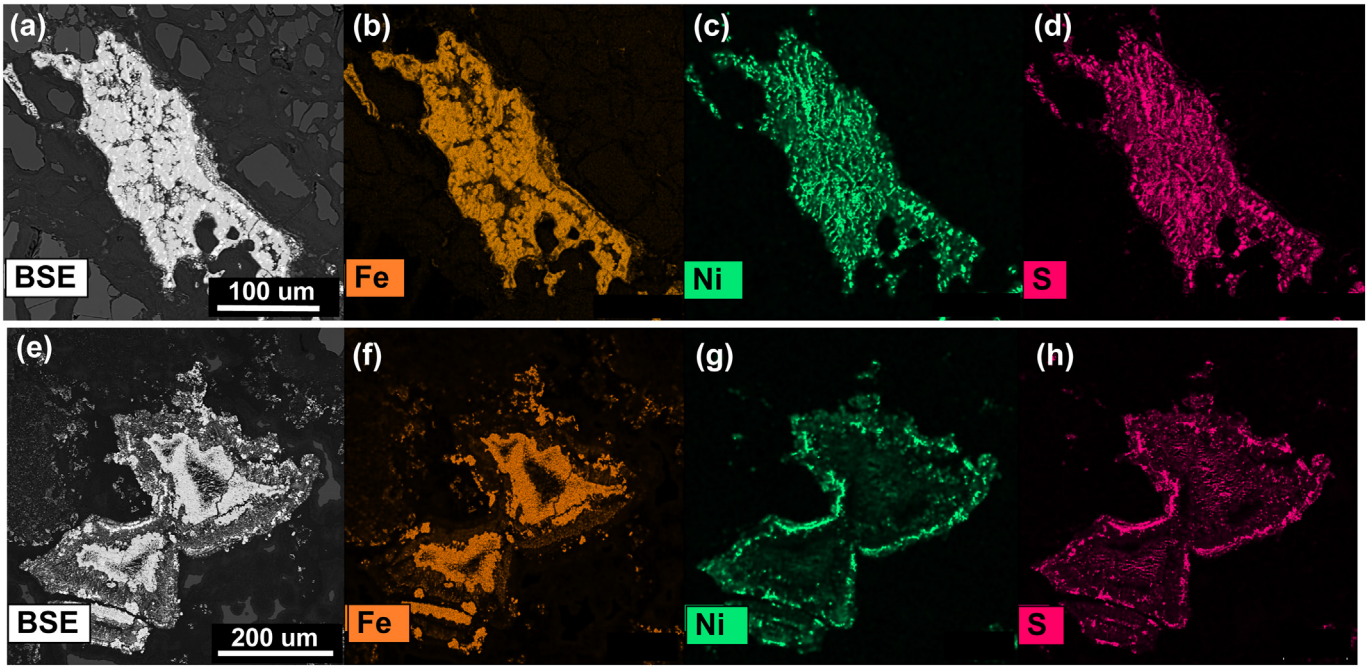

Fig. 6. Back-Scatter Electron (BSE) image (6a, e)and EDS maps showing the Fe (6b, f), Ni (6c,g) and S (6d, h)distribution in two selected sulfides from BD3067.

this is due to the influence of late-stagecrystallising phases but the preservation is also influenced by the anisotropic diffusion of Ni and Cr in olivine.

Most studies that have quantified diffusion of Ni in olivine have used the parameterisation given by Chakraborty (2010)which combines the results of Holzapfel et al. (2007) and Petry et al. (2004). This parameterisation states that both Ni and Fe-Mg diffusion are six times faster along the [001] axis than the [100] and [010] axes. Since Ni diffuses faster along the [001] axis than Fe-Mg, this assumption implies that Ni diffusion should also be faster in the [100] and [010] axes. This relationship was investigated by Spandler and O'Neill (2010) who experimentally determined the relationship between diffusion rate (D) and crystallographic orientation in San Carlos olivine equilibrating with a silicate melt. They published the diffusion coefficients of 19 elements in each of the three principle crystallographic axes.Spandler and O'Neill (2010) showed that there is a strong anisotropy in Ni and Cr diffusion compared to other elements. This is represented in Fig. 10a by the higher gradient in logD for Ni and Cr relative to Fe-Mg and Mn. Ni and Cr diffuse faster along the [001] axis and slower along the [010] axis than Fe-Mg, which magnifies the order of anisotropy. (Ito and Ganguly, 2006) also found Cr to have anisotropic diffusion in olivine. The results of Spandler and O'Neill agree with the parameterisations in Chakraborty (2010) and Dohmen and Chakraborty (2007) for the [001] axis where Ni diffusion is 1.5 times faster than Fe-Mg, but they

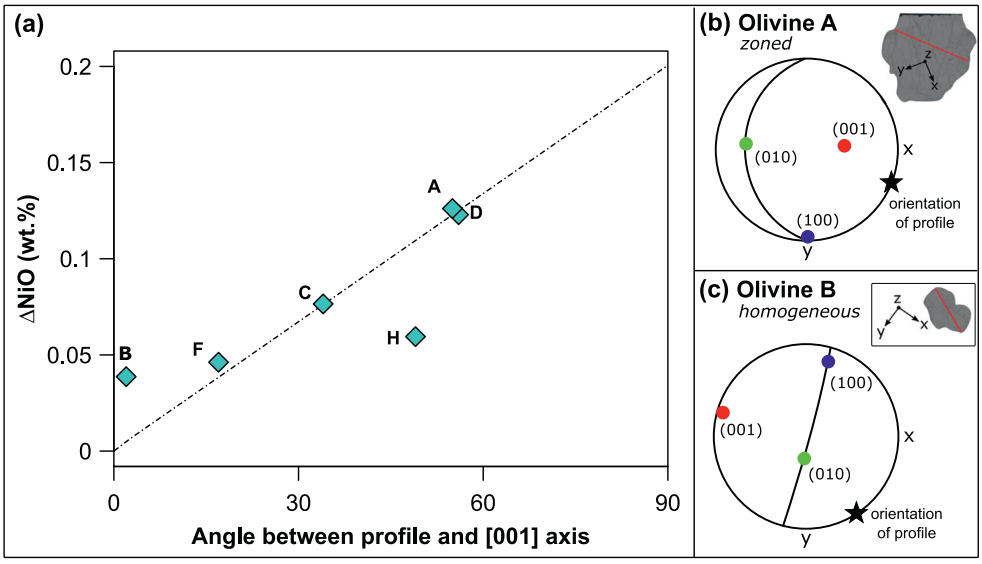

Fig. 7. (a)The range in NiO (ΔNiO) across the profile in each crystal plotted against the orientation of the [001] axis. The position of the [001] is also shown in the stereonet visualisation for (b)Olivine A and (c)Olivine B. Each stereonet shows the plunge and trend of the <100> axes relative to the crystal face and the strike and dip of the (001) plane. The star shows the orientation of the profile analysed.

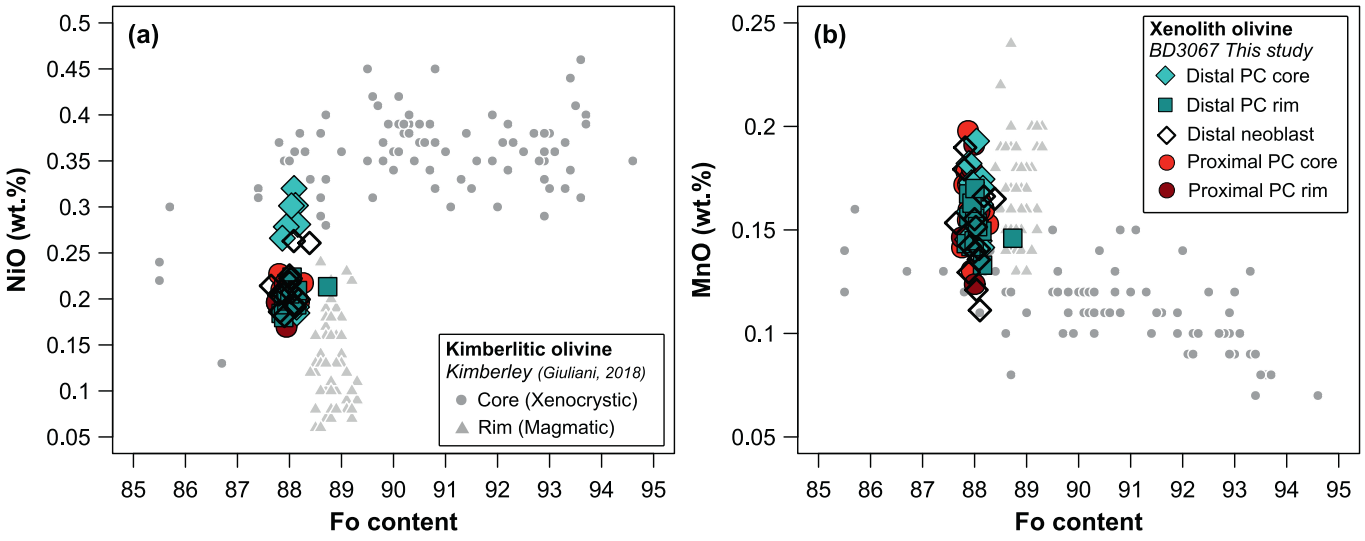

Fig. 8. Forsterite content vs. (a)NiO and (b)MnO for olivines in BD3067 compared to xenocrystic olivine cores and magmatic olivine rims from Kimberlites in the Kimberley region (Giuliani, 2018).

differ in the factor of anisotropy for Ni and Cr. The anisotropy observed by Spandler and O'Neill (2010) is as follows:

$$D^{Ni}_{[001]} = 9D^{Ni}_{[100]} = 11D^{Ni}_{[010]}$$

$$D^{Cr}_{[001]} = 6D^{Cr}_{[100]} = 17D^{Cr}_{[010]}$$

This study highlights the importance of crystallographic orientation as a control on multi-element diffusion in olivine. The observations of isolated Ni and Cr disequilibrium in our study support the implication that their diffusion in olivine is faster in the [001] axis and slower in the [100] and [010] axes, than Fe-Mg, Mn, V, Sc etc. This finding is consistent with other studies in natural volcanic systems which have also inferred that Ni diffusion can be slower than Fe-Mg interdiffusion (e.g. Ruprecht and Plank, 2013; Vinet and Higgins, 2010).

This greater anisotropy in Ni and Cr, relative to other elements, can be explained by their ordering in the olivine crystal structure. Ni is preferentially ordered into the M1 site in olivine, primarily due to its high electronegativity (Bish, 1981; Boström, 1989). The M1 sites form chains parallel to the [001] axis and the preferred diffusion pathway for Ni is along the M1 chains (Miyamoto and Takeda, 1983). As a result, Ni diffuses much faster along the [001] axis than the [100] and [010] axes. The diffusion mechanisms causing the enhanced anisotropy of Cr in olivine are poorly constrained (Ito and Ganguly, 2006) but it is understood that Cr^{3+} orders preferentially onto the M1 sites, and as a result has a stronger anisotropy. Cr^{2+} has an even distribution across M1 and M2 sites and therefore shows less anisotropy than Cr^{3+} (Jollands et al., 2017). Jollands et al. (2017) find a similar level of anisotropy between Cr^{3+} and Ni^{2+}, hence the correlations observed made in this study imply that the majority of Cr in the olivine porphyroclasts is Cr^{3+}.

The anisotropy of M1 ordered elements in olivine can be increased further by silica activity (Jollands et al., 2017; Zhukova et al., 2014). The silica activity (a_{SiO2}) of the melt equilibrating with the olivine impacts the diffusion coefficients of M1 ordered cations because increased a_{SiO2} creates more M1 vacancies, which increases the diffusion rates of

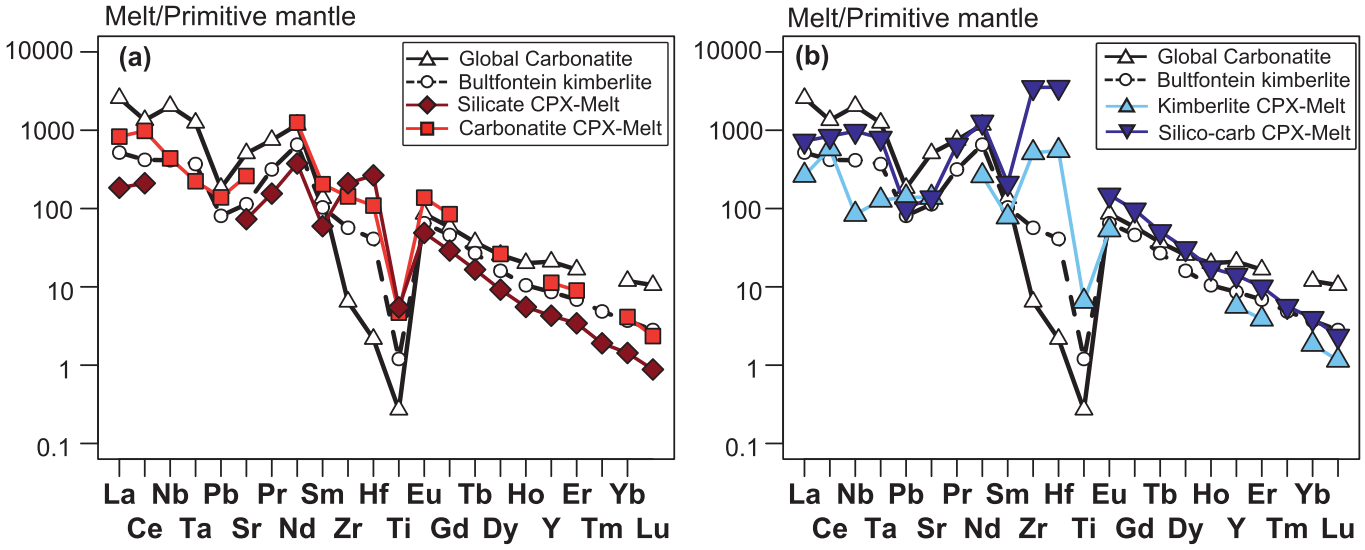

Fig. 9. Primitive mantle normalised trace-element plot comparing the melt in equilibrium with the clinopyroxenes with melt compositions of the host Bultfontein kimberlite (Roex et al., 2003) and a global average carbonatite composition (Bizimis et al., 2003). The four equilibrium melts plotted use(a)cpx-carbonatite melt partition coefficients from Dasgupta et al. (2009) and cpx-silicate melt partition coefficients from Suzuki et al. (2012); and (b)cpx-silicate-carbonate melt partition coefficients from Girnis et al. (2013) and cpx-CO_2-rich kimberlite melt partition coefficients from Keshav et al. (2005). Details of these can be found in Supplementary File D.

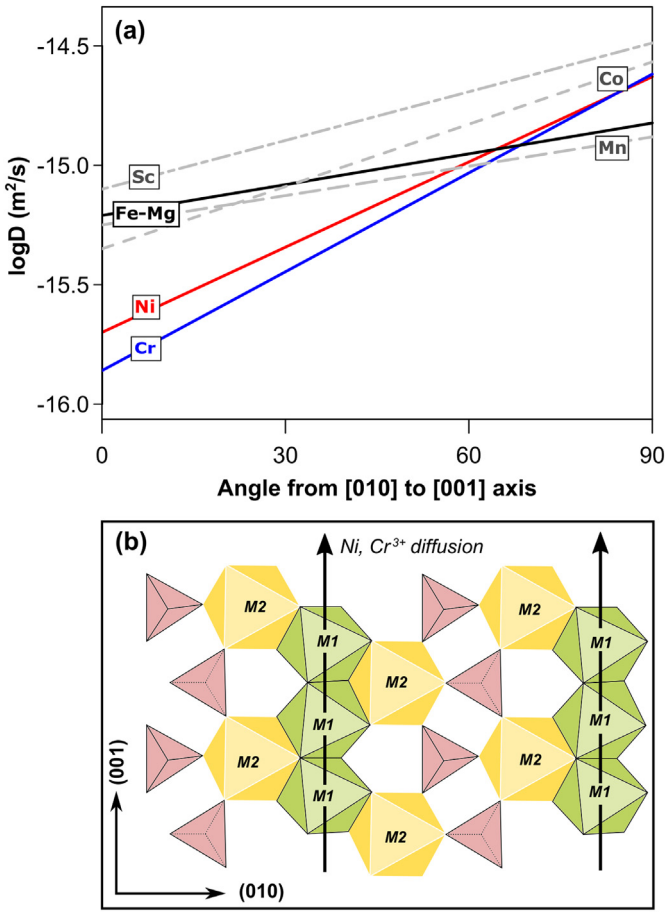

Fig. 10. (a)Diffusion coefficients for a selection of major, minor and trace elements in olivine, between the [010] axis (at 0°) and the [001] axis (at 90°) as determined by Spandler and O'Neill (2010). The elements are labelled on the diagram, including Fe-Mg interdiffusion. The level anisotropy is depicted in the gradient of the line for each element. (b)The olivine structure, showing the position of the M1 and M2 sites relative to the tetrahedra (pink triangle) in the (001) and (010) orientations. The M1 sites form chains parallel to (001), the preferred diffusion pathway for M1 ordered cations, such as Ni and Cr^{3+}, is along these chains.

M1 ordered cations along the [001] axis (Zhukova et al., 2014). Therefore, the low a_{SiO2} of kimberlite and carbonatite magmas is anticipated to decrease diffusion rates of Ni and Cr in olivine by an order of magnitude (Jollands et al., 2017; Zhukova et al., 2014).

The anisotropic diffusion of Ni and Cr in olivine has meant that these elements have been slow to re-equilibrate in the [100] and [010] (and intermediate) slow axes. This interpretation is supported by the correlation between the level of Ni variation and the angle of the crystal relative to the [001] axis (Fig. 7).

7. Timescales of metasomatism

Timescales of metasomatism are generally estimated by dating minerals or modelling diffusion profiles. We have determined a U-Pb age of 84 ± 11 Ma for the large zircon shown in Fig. 1e (see Supplementary File E for details). This indicates that the metasomatism occurred concomitantly with the Late Cretaceous kimberlite activity in Kimberley, including the eruption of the host Bultfontein kimberlite. To improve on this precision we have used the preservation of Ni disequilibrium in the olivine porphyroclasts to estimate the timing of metasomatism relative to the emplacement of the Bultfontein kimberlite. Since much more work has been done on Ni diffusion in olivine than Cr we have opted to only model the Ni diffusion profiles, to estimate the timescales over which the large porphyroclasts would equilibrate with their local mineral assemblage. Our calculations assume that Ni diffusion in the xenolith ceased during kimberlite emplacement and cooling. We have calculated timescales using both the simplistic relationship that the diffusion time (t) is proportional to the distance (x) squared over diffusion rate (D):

$$t \propto x^2/D$$

and we have also modelled the diffusion profiles using the following relationship:

$$C = (C_0 - C_e)\ \mathrm{erf}\left(\frac{X}{2\sqrt{Dt}}\right) + C_e \quad (1)$$

(Crank, 1956) where C_0 is the concentration at the core, C_e is the concentration at the rim, X is the distance from the edge of the crystal, and C is the concentration at position X. In both cases the diffusion coefficient for Ni in the [001] axis was calculated using the following parameterisation:

$$D_{[001]Ni} = 3.84 \times 10^{-9}\left(\frac{fO_2}{10^{-6}}\right)^{1/4.25} 10^{1.5(X_{Fe}-0.1)}\ exp\left(-\frac{220000 + \left(P-10^5\right)\left(7\times10^{-6}\right)}{RT}\right) \quad (2)$$

(Chakraborty, 2010; Holzapfel et al., 2007; Petry et al., 2004)

We considered the anisotropy to be close to the factors established by Spandler and O'Neill (2010), i.e. 10 times slower in the [100] and [001] axes. Another factor we had to account for is that the low silica activity of the metasomatic melt can decrease the diffusion rates. There is no formal parameterisation to take this into consideration for kimberlite melts but based on the conclusions of Zhukova et al. (2014) we have decreased diffusion rates by a factor of 10.

The modelling has been carried out at a range of temperature and pressure conditions appropriate to the Kaapvaal geotherm because the mineral assemblage and chemistry of this xenolith is unsuitable for the application of any standard thermo-barometers. Fig. 11 demonstrates the several orders of magnitude change in equilibration timescales for a 2 mm crystal over the temperature interval 900–1250 °C. The simple calculations show that homogeneity can be achieved within 1 million years even at the low temperature of 900 °C. Our calculations are in good agreement with the diffusion profile modelling, the results of which are shown in Fig. 11b–d. The model suggests that at 1000 °C metasomatism occurred 200,000–300,000 years prior to kimberlite emplacement, and at 1200 °C this decreases to 10,000–20,000 years. This is important because it gives an idea of the extended period of metasomatism by 'failed' kimberlite melts prior to the ascent of the final host kimberlite magma (e.g. Bussweiler et al., 2016; Fitzpayne et al., 2018; Giuliani et al., 2013a; Soltys et al., 2018).

8. Reactive infiltration of proto-kimberlite melts

The sub-continental lithospheric mantle has a complex metasomatic history. We suggest that xenolith BD3067 represents an important period of metasomatism prior to eruption of the kimberlite at the surface. Kimberlite eruptions are enigmatic but it is generally agreed that they consist of pulses of magmatism (e.g. Dawson and Smith, 1977; Field et al., 2009; Giuliani et al., 2016, 2014a; Mitchell, 2008, 1991). Polymict breccias from Bultfontein are interpreted to represent 'failed' kimberlite melts that did not make it to the surface (Giuliani et al., 2013a) and recently Jollands et al. (2018) identified two stages of metasomatism preserved in garnet, the second of which was interpreted as reactive infiltration of a silico-carbonate-rich melt, assumed to be a proto-kimberlite melt. (Woodhead et al., 2017) have identified isotopic homogeneity amongst mantle-derived zircon megacrysts from kimberlites in the Kaapvaal craton, they attribute this to a continent-wide

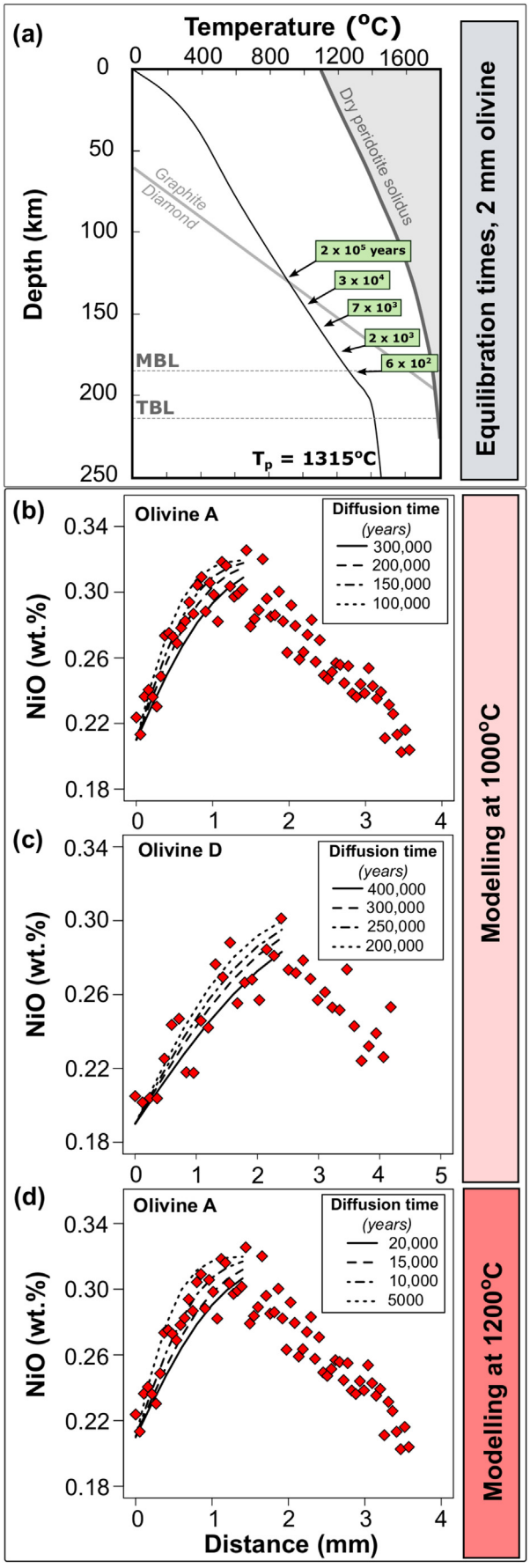

metasomatic event that occurred between 114 Ma and several hundred million years ago. Our work provides evidence for a more localised metasomatic event, associated with the Bultfontein kimberlite, that occurred within half a million years of emplacement.

We suggest that the clinopyroxene vein in BD3067 crystallised during reactive percolation of a very early pulse of proto-kimberlite melt that infiltrated and reacted with harzburgite wall rock. This involved assimilation of orthopyroxene and diffusive exchange with the olivines in the mantle wall rock, together with fractionation of clinopyroxene from the melt (e.g.(Aulbach et al., 2017; Lim et al., 2018; Simon et al., 2003; Tollan et al., 2015). We suggest that the clinopyroxene crystallised during an early stage of fractionation and the changing mineral assemblage created localised concentration gradients that initiated elemental redistribution during subsolidus re-equilibration. At a later stage of fractionation, the residual melt became saturated in sulfur (e.g. Aulbach et al., 2017; Giuliani et al., 2013a). As sulfides precipitated the equilibrium conditions changed again and the introduction of a phase with Ni as a stoichiometric component drove the equilibrating olivine Ni concentration even lower. The Cr concentration of the olivines was affected by the initial fractionation of clinopyroxene and Cr-spinel. Many elements experienced diffusive exchange during metasomatism resulting in complete equilibration, however the lag in Ni and Cr diffusion that we observe in some olivine porphyroclasts has also been influenced by their anisotropic diffusion in olivine.

In this scenario, the newly formed mineral assemblage achieves local equilibrium over time, until another kimberlite pulse utilises the pathway generated by thousands of years of metasomatism to ascend to the surface (Giuliani et al., 2016, 2014a). The rapid, violent ascent of the kimberlite fractures the wall-rock and the metasomatised mantle becomes entrained in the kimberlite. Fig. 12 shows a summary of the metasomatic history of xenolith BD3067.

9. Comparison with previous estimates for the duration of pre-emplacement metasomatism

A number of attempts have been made to constrain the precise timescales of the metasomatism that accompanies kimberlite activity. Most studies have applied diffusion modelling to major- and trace-element disequilibrium in pyrope garnet (Griffin et al., 1996; Smith et al., 1991; Smith and Ehrenberg, 1984), although Konzett et al. (2013) have adopted the same approach to Sr zoning in K-richterite. These studies concluded that metasomatic processes occur on timescales of up to 10^4 years before the eruption of the kimberlite host. Recent modelling of Ni diffusion in garnets by Jollands et al. (2018) suggests that metasomatism by a "failed" kimberlite occurred between 25 days and 400 years prior to host kimberlite entrainment. Giuliani et al. (2013) modelled Ni-rich metasomatism associated with the Bultfontein kimberlite, they present similar profiles to Fig. 5 but show that Ni has diffused into the olivine from Ni-rich melts. Their modelling implies that metasomatism occurred 100 years (at 1000 °C) to 1.7 Myr (at 700 °C) prior to emplacement of the Bultfontein kimberlite.

The ten to hundred thousand year timescales of equilibration estimated in this study are comparable to, or slightly longer than, those derived from previous studies (Cordier et al., 2015; Giuliani et al., 2013; Griffin et al., 1996; Jollands et al., 2018; Smith and Ehrenberg, 1984).

Fig. 11. (a)Bultfontein geotherm (Mather et al., 2011) with annotations to show the relative times required for Ni to diffuse in olivine over 2 mm at various points in the lithosphere, controlled by the temperature. (b-d) Diffusion model showing estimates of times required to achieve the NiO zoning observed in the steepest limbs (hence slowest– gives minimum time) of the profiles in (b) Olivine A at1000 °C; (c) Olivine D 1000 °C and (d) Olivine A at 1200 °C. The diffusion is modelled using the equations of Chakraborty et al. (2010) and Crank et al. (1956) and the method is described in the main text.

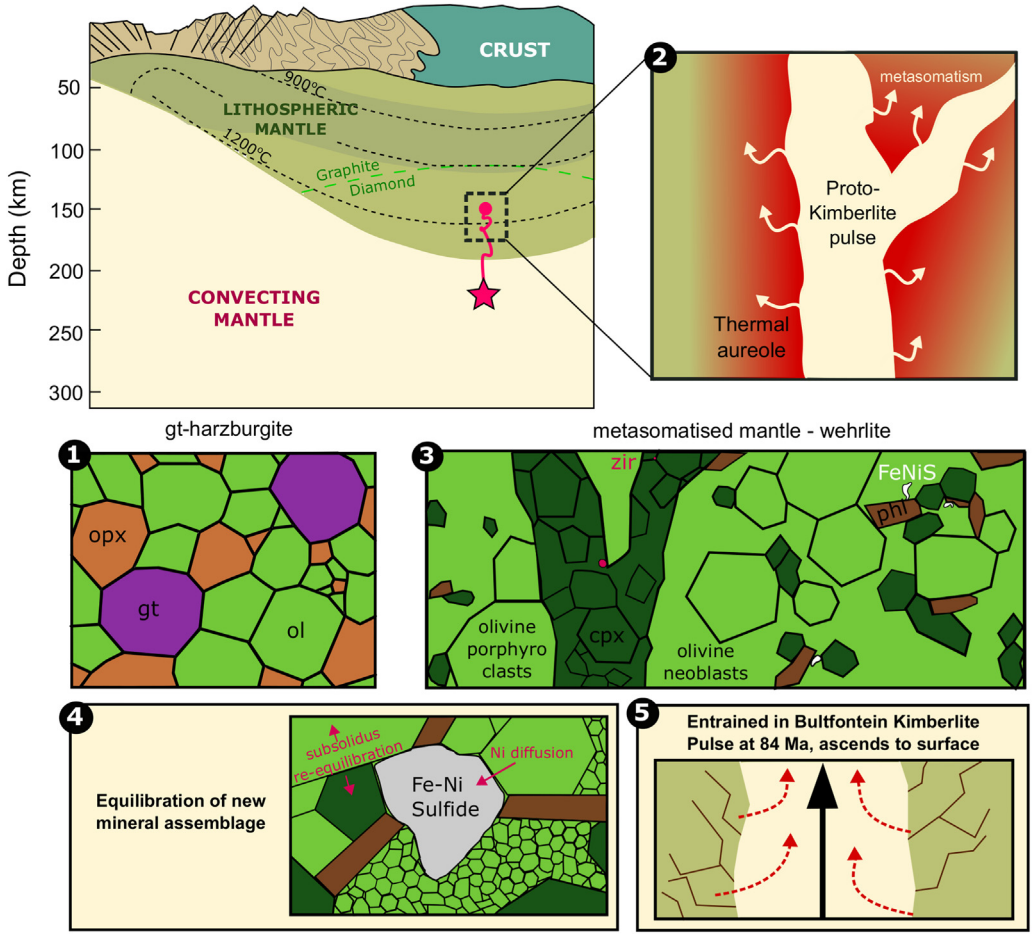

Fig. 12. Schematic diagram summarising the history of the veined xenolith from Bultfontein (BD3067). The emplacement of the Bultfontein kimberlite is preceded by a period of melt infiltration and metasomatism. The metasomatism changes the equilibrium conditions by altering the mineral assemblage. The subsequent re-equilibration takes place over a short timescale, 10^3–10^5 years, and the disequilibrium can be preserved if the xenolith is entrained before equilibration has been achieved.

The olivine disequilibrium related to crystallographic orientation that we observed in our detailed study of BD3067 adds an extra constraint (c.f. garnets that have a more uniform compositional zonation due to their isotropic structure). The range of timescales provided both here and in previous studies supports the hypothesis that a period of metasomatism by 'failed' kimberlite melts precedes the final kimberlite eruption, and that this period is necessary to provide a pathway for the 'successful' kimberlite to exploit (Giuliani et al., 2016, 2014a).

10. Conclusions

Our investigation of the processes associated with the infiltration of metasomatic melts in sub-cratonic lithospheric mantle is focused on a peridotite xenolith that represents a relatively rare, incomplete stage of melt-rock reaction. The xenolith (BD3067), which was brought to the surface by the Late Cretaceous Bultfontein kimberlite (South Africa), contains a spectacular metasomatic vein of diopside, sulfide, phlogopite, spinel and zircon set in a dunite host that we interpret as a relict melt channel. From our detailed petrographic study and systematic in-situmicro-analyses of major, minor and trace elements we conclude that the vein assemblage in BD3067 crystallised from a percolating proto-kimberlite (silico-carbonate) melt. Reactive infiltration of this small-fractionsilica-poor melt appears to have also caused the dissolution of orthopyroxene and precipitation of olivine neoblasts (Fo_{88}).

Unique information on the variable rates of diffusion of major, minor and trace elements during sub-solidusre-equilibration that follows mantle metasomatism is preserved in relict olivine porphyroclasts (Fo_{88}). These have homogeneous concentrations of Mg, Fe and Mn but exhibit significant core to rim decreases in both NiO (0.32–0.18 wt%), and Cr (60–35 ppm). We propose that this heterogeneity is strongly influenced by concentration gradients in Ni and Cr away from the main melt channel and also the localised crystallisation of sulfides and spinel. Our EBSD study of the olivine porphyroclasts shows that Ni and Cr zoning is only evident in grains that contain large components of the [100] and [010] slow diffusion axes.

Diffusion models suggest the preservation of the observed core-to-rim variation of Ni in olivine requires that mantle metasomatism must have occurred within the order of 10^5 years prior to emplacement of the host Bultfontein kimberlite. This metasomatism may have been fundamental to the subsequent ascent and emplacement of the host kimberlite. The time constraint on preservation of core-to-rim variations in Ni and Cr combined with the crystallographic control on diffusion may explain why Ni and Cr heterogeneity in otherwise homogeneous mantle olivine has been so rarely encountered.

A broader implication of our study is that the magnitude of anisotropy in diffusion for Fe-Mg in olivine is different to highly-ordered elements such as Ni, which appear to diffuse much more slowly along the [100] and [010] axes. This is of significance to both mantle and magmatic olivines and highlights the importance for diffusion studies that combine chemical zonation with crystallographic information.

Supplementary data to this article can be found online at https://doi.org/10.1016/j.lithos.2018.08.026.

Acknowledgements

Veined mantle peridotite BD3067 is housed in the JB Dawson collection in the Sedgwick Museum, University of Cambridge. We thank Jason Day for his assistance with LA-ICP-MS analysis, and Iris Buisman and Giulio Lampronti for technical help with EPMA and EBSD, respectively. We are very grateful to Sonja Aulbach and Andrea Giuliani for their constructive reviews of an earlier draft of this manuscript. We acknowledge financial support from NERCRSTG(NE/L002507/1) to CGJ and the Department of Earth Sciences, University of Cambridge, UK.

References

van Achterbergh, E., Griffin, W.L., Stiefenhofer, J., 2001. Metasomatism in mantle xenoliths from the Letlhakane kimberlites: estimation of element fluxes. Contrib. Mineral. Petrol. 141:397–414. https://doi.org/10.1007/s004100000236.

Arndt, N.T., Guitreau, M., Boullier, A.-M., Le Roex, A., Tommasi, A., Cordier, P., Sobolev, A., 2010. Olivine, and the Origin of Kimberlite. J. Petrol. 51:573–602. https://doi.org/10.1093/petrology/egp080.

Aulbach, S., Sun, J., Tappe, S., Höfer, H.E., Gerdes, A., 2017. Volatile-rich metasomatism in the Cratonic mantle beneath SW Greenland: link to kimberlites and mid-lithospheric discontinuities. J. Petrol. 58:2311–2338. https://doi.org/10.1093/petrology/egy009.

Barnes, S.J., Godel, B., Gürer, D., Brenan, J.M., Robertson, J., Paterson, D., 2013. Sulfide-olivineFe-Ni exchange and the origin of anomalously Ni rich magmatic sulfides. Econ. Geol. 108:1971–1982. https://doi.org/10.2113/econgeo.108.8.1971.

Bish, D.L., 1981. Cation ordering in synthetic and natural Ni-Mg olivine. Am. Mineral. 66, 7.

Bizimis, M., Salters, V.J.M., Dawson, J.B., 2003. The brevity of carbonatite sources in the mantle: evidence from Hf isotopes. Contrib. Mineral. Petrol. 145:281–300. https://doi.org/10.1007/s00410-003-0452-3.

Boström, D., 1989. Cation ordering at 1300 C in the (Ni, Mg)-olivine solid solution series. Acta Chem. Scand. 43, 116–120.

Bussweiler, Y., Foley, S.F., Prelević, D., Jacob, D.E., 2015. The olivine macrocryst problem: new insights from minor and trace element compositions of olivine from Lac de Gras kimberlites, Canada. Lithos 220–223:238–252. https://doi.org/10.1016/j.lithos.2015.02.016.

Bussweiler, Y., Stone, R.S., Pearson, D.G., Luth, R.W., Stachel, T., Kjarsgaard, B.A., Menzies, A., 2016. The evolution of calcite-bearing kimberlites by melt-rock reaction: evidence from polymineralic inclusions within clinopyroxene and garnet megacrysts from Lac de Gras kimberlites, Canada. Contrib. Mineral. Petrol. 171 (65). https://doi.org/10.1007/s00410-016-1275-3.

Chakraborty, S., 2010. Diffusion coefficients in Olivine, Wadsleyite and Ringwoodite. Rev. Mineral. Geochem. 72:603–639. https://doi.org/10.2138/rmg.2010.72.13.

Cherniak, D.J., Liang, Y., 2012. Ti diffusion in natural pyroxene. Geochim. Cosmochim. Acta 98, 31–47.

Cherniak, D.J., Liang, Y., 2014. Titanium diffusion in olivine. Geochim. Cosmochim. Acta 147:43–57. https://doi.org/10.1016/j.gca.2014.10.016.

Cordier, C., Sauzeat, L., Arndt, N.T., Boullier, A.-M., Batanova, V., Barou, F., 2015. Metasomatism of the lithospheric mantle immediately precedes Kimberlite eruption: New evidence from olivine composition and microstructures. J. Petrol. 56:1775–1796. https://doi.org/10.1093/petrology/egv054.

Costa, F., Morgan, D., 2010. Time constraints from chemical equilibration in magmatic crystals. Timescales of Magmatic Processes. Wiley-Blackwell:pp. 125–159 https://doi.org/10.1002/9781444328509.ch7.

Crank, J., 1956. The Mathematics of Diffusion. Oxford University Press, Oxford.

Dasgupta, R., Hirschmann, M.M., McDonough, W.F., Spiegelman, M., Withers, A.C., 2009. Trace element partitioning between garnet lherzolite and carbonatite at 6.6 and 8.6 GPa with applications to the geochemistry of the mantle and of mantle-derived melts. Chemical Geology, Volatiles and Volatile-Bearing Melts in the Earth's Interior. 262:pp. 57–77. https://doi.org/10.1016/j.chemgeo.2009.02.004.

Dawson, J.B., 1981. The nature of the upper mantle. Mineral. Mag. 44, 1–18.

Dawson, J.B., 1984. Contrasting types of upper mantle metasomatism. Kimberlites II: The Mantle and Crust-Mantle Relationships. Elsevier, Amsterdam.

Dawson, J.B., Smith, J.V., 1977. The MARID(mica-amphibole-rutile-ilmenite-diopside) suite of xenoliths in kimberlite. Geochim. Cosmochim. Acta 41:309–323. https://doi.org/10.1016/0016-7037(77)90239-3.

De Hoog, J.C.M., Gall, L., Cornell, D.H., 2010. Trace-element geochemistry of mantle olivine and application to mantle petrogenesis and geothermobarometry. Chem. Geol. 270: 196–215. https://doi.org/10.1016/j.chemgeo.2009.11.017.

Dohmen, R., Chakraborty, S., 2007. Fe–Mg diffusion in olivine II: point defect chemistry, change of diffusion mechanisms and a model for calculation of diffusion coefficients in natural olivine. Phys. Chem. Miner. 34:409–430. https://doi.org/10.1007/s00269-007-0158-6.

Erlank, A.J., 1987. Evidence for mantle metasomatism in peridotite nodules from the Kimberley pipes, South Africa. Mantle Metasomatism, pp. 221–311.

Field, M., Gernon, T.M., Mock, A., Walters, A., Sparks, R.S.J., Jerram, D.A., 2009. Variations of olivine abundance and grain size in the Snap Lake kimberlite intrusion, Northwest Territories, Canada: a possible proxy for diamonds. Lithos, Proceedings of the 9th International Kimberlite Conference. 112:pp. 23–35. https://doi.org/10.1016/j.lithos.2009.04.019.

Fitzpayne, A., Giuliani, A., Phillips, D., Hergt, J., Woodhead, J.D., Farquhar, J., Fiorentini, M.L., Drysdale, R.N., Wu, N., 2018. Kimberlite-related metasomatism recorded in MARID and PIC mantle xenoliths. Mineral. Petrol.:1–14 https://doi.org/10.1007/s00710-018-0573-z.

Foley, S.F., Prelevic, D., Rehfeldt, T., Jacob, D.E., 2013. Minor and trace elements in olivines as probes into early igneous and mantle melting processes. Earth Planet. Sci. Lett. 363:181–191. https://doi.org/10.1016/j.epsl.2012.11.025.

Gibson, S.A., Malarkey, J., Day, J.A., 2008. Melt depletion and enrichment beneath the Western Kaapvaal Craton: evidence from Finsch Peridotite Xenoliths. J. Petrol. 49: 1817–1852. https://doi.org/10.1093/petrology/egn048.

Gibson, S.A., McMahon, S.C., Day, J.A., Dawson, J.B., 2013. Highly refractory lithospheric mantle beneath the Tanzanian Craton: evidence from Lashaine pre-metasomaticGarnet-bearing Peridotites. J. Petrol. 54:1503–1546. https://doi.org/10.1093/petrology/egt020.

Girnis, A.V., Bulatov, V.K., Brey, G.P., Gerdes, A., Höfer, H.E., 2013. Trace element partitioning between mantle minerals and silico-carbonate melts at 6–12 GPa and applications to mantle metasomatism and kimberlite genesis. Lithos 160–161: 183–200. https://doi.org/10.1016/j.lithos.2012.11.027.

Giuliani, A., 2018. Insights into kimberlite petrogenesis and mantle metasomatism from a review of the compositional zoning of olivine in kimberlites worldwide. Lithos 312–313:322–342. https://doi.org/10.1016/j.lithos.2018.04.029.

Giuliani, Andrea, Kamenetsky, V.S., Kendrick, M.A., Phillips, D., Goemann, K., 2013. Nickel-rich metasomatism of the lithospheric mantle by pre-kimberliticalkali-S–Cl-rich C–O–H fluids. Contrib. Mineral. Petrol. 165:155–171. https://doi.org/10.1007/s00410-012-0801-1.

Giuliani, A., Kamenetsky, V.S., Kendrick, M.A., Phillips, D., Wyatt, B.A., Maas, R., 2013a. Oxide, sulphide and carbonate minerals in a mantle polymict breccia: metasomatismby proto-kimberlite magmas, and relationship to the kimberlite megacrystic suite. Chemical Geology, Kimberlite, Carbonatite, and Potassic Magmatism as Part of the Geochemical Cycle. 353:pp. 4–18. https://doi.org/10.1016/j.chemgeo.2012.09.025.

Giuliani, A., Phillips, D., Fiorentini, M.L., Kendrick, M.A., Maas, R., Wing, B.A., Woodhead, J.D., Bui, T.H., Kamenetsky, V.S., 2013b. Mantle oddities: a sulphate fluid preserved in a MARID xenolith from the Bultfontein kimberlite (Kimberley, South Africa). Earth Planet. Sci. Lett. 376:74–86. https://doi.org/10.1016/j.epsl.2013.06.028.

Giuliani, A., Phillips, D., Kamenetsky, V.S., Kendrick, M.A., Wyatt, B.A., Goemann, K., Hutchinson, G., 2014a. Petrogenesis of mantle Polymict Breccias: insights into mantle processes coeval with kimberlite magmatism. J. Petrol. 55:831–858. https://doi.org/10.1093/petrology/egu008.

Giuliani, A., Phillips, D., Maas, R., Woodhead, J.D., Kendrick, M.A., Greig, A., Armstrong, R.A., Chew, D., Kamenetsky, V.S., Fiorentini, M.L., 2014b. LIMA U–Pb ages link lithospheric mantle metasomatism to Karoo magmatism beneath the Kimberley region, SouthAfrica. Earth Planet. Sci. Lett. 401:132–147. https://doi.org/10.1016/j.epsl.2014.05.044.

Giuliani, A., Phillips, D., Woodhead, J.D., Kamenetsky, V.S., Fiorentini, M.L., Maas, R., Soltys, A., Armstrong, R.A., 2015. Did diamond-bearing orangeites originate from MARID-veined peridotites in the lithospheric mantle? Nat. Commun. 6 (6837). https://doi.org/10.1038/ncomms7837.

Giuliani, A., Phillips, D., Kamenetsky, V.S., Goemann, K., 2016. Constraints on kimberlite ascent mechanisms revealed by phlogopite compositions in kimberlites and mantle xenoliths. Lithos 240–243:189–201. https://doi.org/10.1016/j.lithos.2015.11.013.

Giuliani, A., Soltys, A., Phillips, D., Kamenetsky, V.S., Maas, R., Goemann, K., Woodhead, J.D., Drysdale, R.N., Griffin, W.L., 2017. The final stages of kimberlite petrogenesis: Petrography, mineral chemistry, melt inclusions and Sr-C-O isotope geochemistry of the Bultfontein kimberlite (Kimberley, South Africa). Chemical Geology, The role of intra-plate magmas and their inclusions in Earth's mantle evolution. 455:pp. 342–356. https://doi.org/10.1016/j.chemgeo.2016.10.011.

Griffin, W.L., Smith, D., Ryan, C.G., O'Reilly, S.Y., Win, T.T., 1996. Trace-element zoning in mantle minerals; metasomatism and thermal events in the upper mantle. Can. Mineral. 34, 1179–1193.

Griffin, W.L., Batumike, J.M., Greau, Y., Pearson, N.J., Shee, S.R., O'Reilly, S.Y., 2014. Emplacement ages and sources of kimberlites and related rocks in southern Africa: U–Pb ages and Sr–Nd isotopes of groundmass perovskite. Contrib. Mineral. Petrol. 168 (1032). https://doi.org/10.1007/s00410-014-1032-4.

Harte, B., 1983. Mantle peridotites and processes: the kimberlite sample. In: Hawkesworth, C.J., Norry, M.J., Shiva, Nantwich (Eds.), Continental Basalts and Their Xenoliths. Shiva, Nantwich.

Holzapfel, C., Chakraborty, S., Rubie, D.C., Frost, D.J., 2007. Effect of pressure on Fe–Mg, Ni and Mn diffusion in $(Fe_xMg_{1-x})_2SiO_4$ olivine. Phys. Earth Planet. Inter. 162:186–198. https://doi.org/10.1016/j.pepi.2007.04.009.

Ito, M., Ganguly, J., 2006. Diffusion kinetics of Cr in olivine and 53Mn–53Cr thermochronology of early solar system objects. Geochim. Cosmochim. Acta 70: 799–809. https://doi.org/10.1016/j.gca.2005.09.020.

Jollands, M.C., O'Neill, H.S.C., Van Orman, J., Berry, A.J., Hermann, J., Newville, M., Lanzirotti, A., 2017. Substitution and diffusion of Cr^{2+} and Cr^{3+} in synthetic forsterite and natural olivine at 1200–1500 °C and 1 bar. Geochim. Cosmochim. Acta https://doi.org/10.1016/j.gca.2017.09.030.

Jollands, M.C., Hanger, B.J., Yaxley, G.M., Hermann, J., Kilburn, M.R., 2018. Timescales between mantle metasomatism and kimberlite ascent indicated by diffusion profiles in garnet crystals from peridotite xenoliths. Earth Planet. Sci. Lett. 481, 143–153.

Jones, A.P., Smith, J.V., Dawson, J.B., 1982. Mantle Metasomatism in 14 Veined Peridotites from Bultfontein Mine, South Africa. J. Geol. 90, 435–453.

Keshav, S., Corgne, A., Gudfinnsson, G.H., Bizimis, M., McDonough, W.F., Fei, Y., 2005. Kimberlite petrogenesis: Insights from clinopyroxene-melt partitioning experiments at 6 GPa in the $CaO-MgO-Al_2O_3-SiO_2-CO_2$ system. Geochim. Cosmochim. Acta 69: 2829–2845. https://doi.org/10.1016/j.gca.2005.01.012.

Kinny, P.D., Dawson, J., 1992. A mantle metasomatic injection event linked to late Cretaceous kimberlite magmatism. Nature 360.

Konzett, J., Armstrong, R.A., Sweeney, R.J., Compston, W., 1998. The timing of MARID metasomatism in the Kaapvaal mantle: an ion probe study of zircons from MARID xenoliths. Earth Planet. Sci. Lett. 160:133–145. https://doi.org/10.1016/S0012-821X(98)00073-9.

Konzett, J., Armstrong, R.A., Günther, D., 2000. Modal metasomatism in the Kaapvaal craton lithosphere: constraints on timing and genesis from U–Pb zircon dating of metasomatized peridotites and MARID-type xenoliths. Contrib. Mineral. Petrol. 139, 704–719.

Konzett, J., Wirth, R., Hauzenberger, C., Whitehouse, M., 2013. Two episodes of fluid migration in the Kaapvaal Craton lithospheric mantle associated with cretaceous kimberlite activity: evidence from a harzburgite containing a unique assemblage of metasomatic zirconium-phases. Lithos 182–183:165–184. https://doi.org/10.1016/j.lithos.2013.10.005.

Kramers, J.D., Roddick, J.C.M., Dawson, J.B., 1983. Trace element and isotope studies on veined, metasomatic and "MARID" xenoliths from Bultfontein, South Africa. Earth Planet. Sci. Lett. 65:90–106. https://doi.org/10.1016/0012-821X(83)90192-9.

Leitch, C., Steele, I., Hutcheon, I., Smith, J.V., 1979. Minor elements in pallasites: zoning in springwater olivine. Lunar Planet. Sci. X 716–718.

Liati, A., Franz, L., Gebauer, D., Fanning, C.M., 2004. The timing of mantle and crustal events in South Namibia, as defined by SHRIMP-dating of zircon domains from a garnet peridotite xenolith of the Gibeon Kimberlite Province. J. Afr. Earth Sci. Key Points Afr. Geol. 39:147–157. https://doi.org/10.1016/j.jafrearsci.2004.07.054.

Lim, E., Giuliani, A., Phillips, D., Goemann, K., 2018. Origin of complex zoning in olivine from diverse, diamondiferous kimberlites and tectonic settings: Ekati (Canada), Alto Paranaiba (Brazil) and Kaalvallei (South Africa). Mineral. Petrol.:1–16 https://doi.org/10.1007/s00710-018-0607-6.

Lorand, J.-P., Grégoire, M., 2006. Petrogenesis of base metal sulphide assemblages of some peridotites from the Kaapvaal craton (South Africa). Contrib. Mineral. Petrol. 151:521. https://doi.org/10.1007/s00410-006-0074-7.

Mather, K.A., Pearson, D.G., McKenzie, D., Kjarsgaard, B.A., Priestley, K., 2011. Constraints on the depth and thermal history of cratonic lithosphere from peridotite xenoliths, xenocrysts and seismology. Lithos 125:729–742. https://doi.org/10.1016/j.lithos.2011.04.003.

McDonough, W.F., Sun, S.-s., 1995. The composition of the Earth. Chem. Geol. Chem. Evol. Mantle 120:223–253. https://doi.org/10.1016/0009-2541(94)00140-4.

McKenzie, D., 1989. Some remarks on the movement of small melt fractions in the mantle. Earth Planet. Sci. Lett. 95:53–72. https://doi.org/10.1016/0012-821X(89)90167-2.

Menzies, M., Hawkesworth, C., 1986. Mantle metasomatism.

Mitchell, R.H., 1991. Kimberlites and lamproites: primary sources of diamond. Geosci. Can. 18.

Mitchell, R.H., 2008. Peridotite xenoliths and the dynamics of kimberlite intrusion -the mantle sample: inclusion in kimberlites and other volcanics - mercier - Wiley online library. J. Volcanol. Geotherm. Res. 174.

Miyamoto, M., Takeda, H., 1983. Atomic diffusion coefficients calculated for transition metals in olivine. Nature 303, 602–603.

O'Reilly, S.Y., Griffin, W.L., 2013. Mantle metasomatism. Metasomatism and the Chemical Transformation of Rock. Springer, pp. 471–533.

Pearson, D.G., 1995. Re-Os, Sm-Nd, and Rb-Sr isotope evidence for thick Archaean lithospheric mantle beneath the Siberian craton modified by multistage metasomatism. Geochim. Cosmochim. Acta 59:959–977. https://doi.org/10.1016/0016-7037(95)00014-3.

Pearson, D.G., Canil, D., Shirey, S.B., 2003. Mantle samples included in volcanic rocks: xenoliths and diamonds. Treat. Geochem. 2:568. https://doi.org/10.1016/B0-08-043751-6/02005-3.

Petry, C., Chakraborty, S., Palme, H., 2004. Experimental determination of Ni diffusion coefficients in olivine and their dependence on temperature, composition, oxygen fugacity, and crystallographic orientation. Geochim. Cosmochim. Acta 68:4179–4188. https://doi.org/10.1016/j.gca.2004.02.024.

Pilbeam, L.H., Nielsen, T.F.D., Waight, T.E., 2013. Digestion fractional crystallization (DFC): an important process in the genesis of kimberlites. Evidence from olivine in the Majuagaa kimberlite, Southern West Greenland. J. Petrol. 54:1399–1425. https://doi.org/10.1093/petrology/egt016.

Rehfeldt, T., Jacob, D.E., Carlson, R.W., Foley, S.F., 2007. Fe-rich Dunite Xenoliths from South African Kimberlites: Cumulates from Karoo Flood Basalts. J. Petrol. 48: 1387–1409. https://doi.org/10.1093/petrology/egm023.

Roex, A.P.L., Bell, D.R., Davis, P., 2003. Petrogenesis of group I kimberlites from Kimberley, South Africa: evidence from bulk-rock geochemistry. J. Petrol. 44:2261–2286. https://doi.org/10.1093/petrology/egg077.

Rudnick, R.L., McDonough, W.F., Chappell, B.W., 1993. Carbonatite metasomatism in the northern Tanzanian mantle: petrographic and geochemical characteristics. Earth Planet. Sci. Lett. 114:463–475. https://doi.org/10.1016/0012-821X(93)90076-L.

Ruprecht, P., Plank, T., 2013. Feeding andesitic eruptions with a high-speed connection from the mantle. Nature 500, 68–72.

von Seckendorff, V., O'Neill, H.S.C., 1993. An experimental study of Fe-Mg partitioning between olivine and orthopyroxene at 1173, 1273 and 1423 K and 1.6 GPa. Contrib. Mineral. Petrol. 113:196–207. https://doi.org/10.1007/BF00283228.

Shu, Q., Brey, G.P., 2015. Ancient mantle metasomatism recorded in subcalcic garnet xenocrysts: Temporal links between mantle metasomatism, diamond growth and crustal tectonomagmatism. Earth Planet. Sci. Lett. 418:27–39. https://doi.org/10.1016/j.epsl.2015.02.038.

Simon, N.S.C., Irvine, G.J., Davies, G.R., Pearson, D.G., Carlson, R.W., 2003. The origin of garnet and clinopyroxene in "depleted" Kaapvaal peridotites. Lithos, A Tale of Two Cratons: The Slave-Kaapvaal Workshop. 71:pp. 289–322. https://doi.org/10.1016/S0024-4937(03)00118-X.

Simon, N.S.C., Carlson, R.W., Pearson, D.G., Davies, G.R., 2007. The Origin and evolution of the Kaapvaal cratonic lithospheric mantle. J. Petrol. 48:589–625. https://doi.org/10.1093/petrology/egl074.

Smith, D., Ehrenberg, S.N., 1984. Zoned minerals in garnet peridotite nodules from the Colorado Plateau: implications for mantle metasomatism and kinetics. Contrib. Mineral. Petrol. 86:274–285. https://doi.org/10.1007/BF00373673.

Smith, D., Griffin, W.L., Ryan, C.G., Sie, S.H., 1991. Trace-element zonation in garnets from the Thumb: heating and melt infiltration below the Colorado Plateau. Contrib. Mineral. Petrol. 107:60–79. https://doi.org/10.1007/BF00311185.

Soltys, A., Giuliani, A., Phillips, D., 2018. A new approach to reconstructing the composition and evolution of kimberlite melts: a case study of the archetypal Bultfontein kimberlite (Kimberley, South Africa). Lithos 304–307:1–15. https://doi.org/10.1016/j.lithos.2018.01.027.

Spandler, C., O'Neill, H.S.C., 2010. Diffusion and partition coefficients of minor and traceelements in San Carlos olivine at 1300 °C with some geochemical implications. Contrib. Mineral. Petrol. 159:791–818. https://doi.org/10.1007/s00410-009-0456-8.

Stosch, H.-G., 1981. Sc, Cr, Co and Ni partitioning between minerals from spinel peridotitexenoliths. Contrib. Mineral. Petrol. 78:166–174. https://doi.org/10.1007/BF00373778.

Suzuki, T., Hirata, T., Yokoyama, T.D., Imai, T., Takahashi, E., 2012. Pressure effect on element partitioning between minerals and silicate melt: Melting experiments on basalt up to 20 GPa. Phys. Earth Planet. Inter. 208–209:59–73. https://doi.org/10.1016/j.pepi.2012.07.008.

Tollan, P.M.E., O'Neill, H.S.C., Hermann, J., Benedictus, A., Arculus, R.J., 2015. Frozen melt–rock reaction in a peridotite xenolith from sub-arc mantle recorded by diffusion of trace elements and water in olivine. Earth Planet. Sci. Lett. 422:169–181. https://doi.org/10.1016/j.epsl.2015.03.055.

Vinet, N., Higgins, M.D., 2010. Magma solidification processes beneath Kilauea volcano, Hawaii: a quantitative textural and geochemical study of the 1969–1974 Mauna Ulu Lavas. J. Petrol. 51:1297–1332. https://doi.org/10.1093/petrology/egq020.

Witt-Eickschen, G., O'Neill, H.S.C., 2005. The effect of temperature on the equilibrium distribution of trace elements between clinopyroxene, orthopyroxene, olivine and spinel in upper mantle peridotite. Chem. Geol. 221:65–101. https://doi.org/10.1016/j.chemgeo.2005.04.005.

Woodhead, J., Hergt, J., Giuliani, A., Phillips, D., Maas, R., 2017. Tracking continental-scale modification of the Earth's mantle using zircon megacrysts. Geochem. Perspect. Lett.: 1–6 https://doi.org/10.7185/geochemlet.1727.

Zhou, Y., Steele, I., 1993. Chemical zoning and diffusion of Ca, Al, Mn, and CR in olivine of springwater pallasite. Lunar and Planetary Inst., Twenty-Fourth Lunar and Planetary Science Conference. Part 3. Presented at the Lunar and Planetary Inst., Twenty-Fourth Lunar and Planetary Science Conference. Part 3.

Zhukova, I., O'Neill, H.S., Cambell, I.H., Kilburn, M.R., 2014. The effect of silica activity on the diffusion of Ni and Co in olivine. Contrib. Mineral. Petrol. 168 (1029). https://doi.org/10.1007/s00410-014-1029-z.